Spring 2018

The role of flexural slip in the development of chevron folds

Yuxing Wu

Department:

THE ROLE OF FLEXURAL SLIP IN THE DEVELOPMENT OF CHEVRON FOLDS

by

YUXING WU

A THESIS

Presented to the Faculty of the Graduate School of the

MISSOURI UNIVERSITY OF SCIENCE AND TECHNOLOGY

In Partial Fulfillment of the Requirements for the Degree

MASTER OF SCIENCE IN PETROLEUM ENGINEERING

2018

Approved by

Andreas Eckert, Advisor
John Patrick Hogan
Jonathan Obrist Farner

ABSTRACT

Chevron folds are characterized by straight limbs and narrow hinge zones. One of the conceptual models to initiate and develop chevron folds involves flexural slip during folding. While some kinematical models show the necessity for slip to initiate during chevron folding, recent numerical modeling studies of visco-elastic effective single layer buckle folding have shown that flexural slip does not result in chevron folds. In this study, several 2D finite element analysis models are run, distinguished by 1) geometry of the initial perturbation (sinusoidal and white noise), 2) varying thewavelength of the initial perturbation (10%, 50%, and 100% of the dominant wavelength) and 3) variation of the friction coefficient (high and low friction coefficient between interlayers). All numerical simulations apply 60% of shortening, in order to achieve inter-limb angles of 60 to 70 degrees.

The results show that for sinusoidal initial perturbations, systematic and symmetric chevron folds are reproduced when 10% of the dominant wavelength is used for the initial perturbation. Using 50% or 100% of the dominant wavelength results in circular and sinusoidal folds, respectively. Low friction coefficient models result in larger amplitudes and sharper inter-limb angles compared to high friction coefficient models. For white noise initial perturbations, isolated and asymmetric chevron folds are developed when the friction coefficient is low. High friction coefficient models reproduce the dominant wavelength without chevron folds and low friction coefficient models result in a different dominant wavelength. In all chevron folds models, slip initiates at the early stages of folding (i.e. 1% to 5% of shortening).

ACKNOWLEDGMENTS

I would like to thank my advisor, Dr. Andreas Eckert, for giving me the chance to work in the Numerical Geomechanics Research Group. He was an excellent professor and mentor, contributing with my intellectual and personal development. His technical writing guidance was primordial on the development of this work. My gratitude to my committee members, Dr. Hogan and Dr. Obrist Farner that helped me to improve my presentation skills and guide my researches.

I would like to also thank to Zhipeng Zhu, Wangchuchu Han, and Yashu Chen going through my hardest days in the USA. We all came from the same university in China and helped each other so far as possible. Because of them, I met lots of friends in Rolla that was my brothers and sisters on the past years, always helping me with whatever I needed. Thanks Weicheng Zhang and Jianbo Liu for the sincere friendship. We had many talks about how to change the world and he also gave me a lot of guide when I start my research.

Thanks to my roommates, Kailun Ba, and my good friend, Dongyu Zheng, for being such good friends and companies. My partners in the Numerical Geomechanics Research Group, William Chandonia, Avery Welker, Chao Liu and Nso Petter, they helped me a lot in the research and for the good times. Thanks to my good friend, Wenyu Zhao, he taught me a lot of maintaining a strong body and the correct ways to workout. I am also grateful to all the friends that at some point participated on this journey, even though not listed here.

TABLE OF CONTENTS

Page

LIST OF ILLUSTRATIONS

LIST OF TABLES

1. INTRODUCTION

1.1. LITERATURE REVIEW

Chevron folds are a kind of special folding phenomena featuring straight limbs, a narrow and sharp hinge zone and always require a shortening of at least 50 percent (Ramsay and Huber, 1987; Hudleston, 1973; Ryan and Smith, 1998). The speed of development of folding starts slowly but increase rapidly, then reduces in the late stage (Ramsay, 1974). Previous studies have shown that either flexural slip, material anisotropy, or the hinge migration of kink bands or box folds can lead to the development of chevron folds (Twiss, 1973; Ramsay, 1974; Price and Cosgrove, 1990).

Flow anisotropy is a preferred method to describe shape changes in folds. Anisotropic viscosity affects folding structures by controlling flow characteristics (Price and Cosgrove, 1990; Weijermars, 1992). An anisotropic single-layer fold may be described as many isotropic sublayers combined together (Lan and Hudleston, 1996). Effective anisotropy is represented by viscosities of sublayers and their fractional thicknesses (Biot, 1965; Price and Cosgrove, 1990; Lan and Hudleston, 1996). With increasing anisotropy, limbs will be straighter and a narrow, sharper hinge zone will be formed (Bayly, 1970; Cobbold, 1976; Lan and Hudleston, 1996).

Biot, 1965, declared that the hinge zone migration of kink bands or box folds is an alternative method in the development of chevron folds. Laboratory results (Cobbold et al., 1971, Honea and Johnson, 1976; Blay et al., 1977) and numerical modelling studies (Latham, 1985; Ridley and Casey, 1989) are in agreement with the theoretical conclusions.

Hinge migration rates affect the ratio of interlimb angle changing rate to median segment length reduction during buckling (Fowler and Winsor, 1995).

Flexural slip has been recognized as another important mechanism in the evolution of chevron folds (de Sitter, 1958; Ramsay, 1974; Tanner, 1989; Hudleston et al., 1996). Multilayer chevron shaped buckle folds from goldfields in the Bendigo-Castlemaine region in southeastern Australia are good examples of flexural slip, evidenced by laminated veins (Fowler and Winsor, 1997). The evidences show that many individual layers consist of slip and the thicknesses of the beds are around 10 m. The length of the folds limbs are 300 to 400 m, which can be concluded that the ratio of the thicknesses of layers involved slip to the limb length is less than 1/100. (Fowler and Winsor, 1997, Ryan and Smith, 1998, Pollard & Fletcher, 2005) The assumption of flexural slip folding is that slip occurs between competent and competent layers or alternative competent and incompetent layers (Behzadi and Dubey, 1980; William, 1980; Ramsay and Huber, 1987). Numerical simulation results show that flexural slip dominates in low viscosity contrast multilayer folding (Damasceno et al., 2017). Otherwise, flexural flow results in interlayer layer-parallel simple shear strain dominating in the incompetent layers rather than flexural slip on layer surfaces (Ramsay, 1967; Sanz et al., 2008). If the rock materials are all competent, as interlimb angle decreases with fold evolution, the friction between layers increases to resist slip so that most flexural slip folding locks up when the interlimb angle is larger than 60 degrees (Ramsay, 1974; de Sitter, 1958; Tanner, 1989). Plasticine models also demonstrate that flexural slip contributes dominantly at the beginning of folding. At the late stage (interlimb angle equals 60 degree), only small amounts of slip occurred (Behzadi and Dubey, 1980).

Ramsay (1967) stated that the dip and thickness of folding layers control the amount of slip due to the relationship between finite shear strains and dip angle. However, this relationship cannot explain orthogonal thickness changes in chevron fold layers, for example, limb thinning or hinge thickening. Behzadi and Dubey (1980) used laboratory data to conclude that the amount of flexural slip varies in limbs and hinge zones of general flexural folding. According to bedding vein thicknesses in the Bendigo-Castlemaine folds, slip also varies between limb to limb and anticlinal hinge zones (Fowler and Winsor, 1997). In addition, the theory proposed by Ramsay (1974) and Tanner (1989) agrees that the amount of slip attains maximum value at inflexion points of limbs and approaches zero at the hinge zones of general flexural folding in a qualitative manner as well. The quantitative explanation of distributions of flexural slip in chevron folds is still needed.

The strain patterns in single layer chevron folds have been introduced clearly (Bastida et al., 2007). Many field cases show that strain distribution in multilayers chevron folds needs to be investigated to understand the role of flexural slip in the evolution of chevron folds. Some researchers (Behzadi and Dubey, 1980) assumed that flexural slip occur at all layer contacts during visco-elastic buckle folding, but Bendigo-Castlemaine folds (Fowler and Winsor, 1997) and other natural phenomena and theory support that some bedding contact surfaces remain welded together while folding to chevron shape (Tanner, 1989; Horne and Culshaw, 2001). In addition, the slip occurs sequentially and hierarchically. When there is an active slip surface, elongational and contractional strain exists and is expressed by fractures as new slip surfaces develop (Couples et al. 1998).

Many authors evaluate the controlling mechanisms of flexural slip folding shape. Confining pressure results in wavelength changing positively (Johnson and Honea, 1975,

Colman-sadd, 1978) and dominant wavelength affects folding amplitude growth rate (Price and Cosgrove, 1990; Schmid and Podladchikov, 2005). While most conclusions are based on mathematical models, field phenomena, shape evaluation, flexural slip amount and occurrence time, it is hard to exhibit these quantitatively. Numerical models provide a powerful tool to determine the mechanism influences directly and visually. Studies of buckling folds with flexural slip show that friction coefficients have negative effects on slip magnitude and slip occurs at the beginning of folding (Damasceno, 2017). Little research focuses on chevron folds with flexural slip.

Although flexural slip is always recognized as an important mechanism of chevron folds, similar-stiffness compressional multilayer folding with flexural slip did not generate chevron folds in Damasceno's (2017) results. This paper focuses on the flexural slip mechanism in chevron fold development through numerical models to compare with flexural slip in buckling folds in order to generate chevron folding mechanisms. A multilayer model is selected as the initial model setup because a greater number of competent layers makes the model tend toward flexural slip (Hudleston et al., 1996). Several parameters such as friction coefficient, permeability, overburden, and initial perturbation, are discussed to operate the sensitivity analysis for understanding flexural slip in chevron folds evolution.

1.2. RESEARCH OBJECTIVES AND QUESTIONS

Multilayer chevron folds are characterized by narrow hinge zones and straight fold limbs (Hudleston, 1973; Ramsay and Huber, 1987; Fletcher and Pollard, 1999) and are observed in many outcrops in the field (e.g., Chappell and Spang, 1974; Boulter, 1979;

Tanner, 1989, 1992; Fowler and Winsor, 1996; Horne and Culshaw, 2000). The most common model for the development of chevron folds involves buckling of multilayers of alternating competence (De Sitter, 1956, 1964; Bayly, 1964, 1976, Hills, 1972; Ramsay, 1967, 1974; Ghosh, 1968; Chapple, 1969, 1970; Johnson and Honea, 1975; Dubey and Cobbold, 1977; Behzadi and Dubey, 1980; Tanner, 1989; Price and Cosgrove, 1990; Fowler and Winsor, 1996; Hudleston et al., 1996; Fletcher and Pollard, 1999; Pollard and Fletcher, 2005). This is referred to as an effectively anisotropic medium, and any in-plane offset between the competent layers is accommodated by simple shear in the incompetent layers. For an effective single layer setup where the multilayer consists of competent layers only (Schmid and Podladchikov, 2006), several kinematic models for the development of chevron folds account for the contribution of flexural slip between the competent layers (De Sitter, 1964; Pollard and Fletcher, 2005). Field observations in the Bendigo-Castlemaine goldfields, Victoria, Australia (Fowler and Winsor, 1996, 1997; Ryan and Smith, 1998) and in the Meguma Group, Nova Scotia, Canada (Horne and Culshaw, 2000) are good examples of flexural slip chevron folds, because of the presence of offset laminated veins.

The rigid layer slip model by De Sitter (1964), and later adopted by Ramsay (1974), is based on the rotation and the associated slip of rigid layers of equal thickness. The model assumes initial seed folds of chevron shape (before buckling occurs) that have low limb dip angles and broken hinges (Figure 1.1a). During buckling, the upper layer slides relative to the base layer, then all layers rotate equiangular (Figure 1.1 b). As the inter-limb angle decreases with fold evolution, the friction between layers increases to resist slip and the

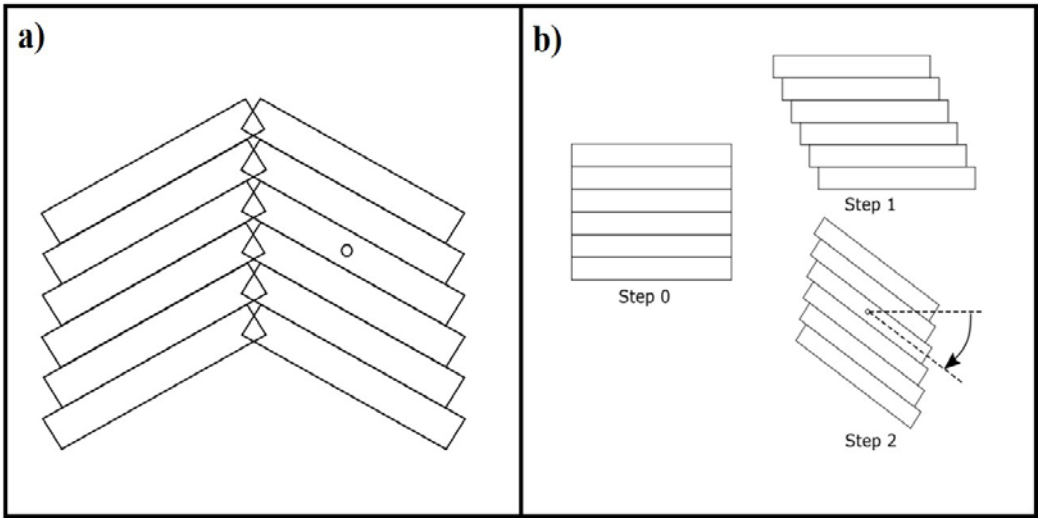

Figure 1.1. Kinematic model of effective single layer. (a) De Sitter (1964) model with low limb dip angles and broken hinges for multilayer chevron folding. The circle acts as the center of rotation for the layer. (b) Two steps to form limbs of chevron fold.

layers lock up when the inter-limb angle rotates to the critical inter-limb angle (approximately 60°) (De Sitter, 1964; Ramsay, 1974; Tanner, 1989).Since the chevron folds observed by Fowler and Winsor, 1996) and by Horne and Culshaw (2000) in addition to flexural slip also feature cleavage, Pollard and Fletcher (2005) propose a combination of a homogeneous flattening model (which accounts for the development of cleavage without slip) and a rigid layer slip model (which by itself does not account for cleavage). The model starts with a rigid layer slip model, and as the limb dip increases during layer rotation and interlayer slip in the initial stages of deformation, it transforms to the homogeneous flattening model without slip in the later stages to generate chevron folds with vertical cleavage. This model can be used to explain the observation of chevron folds in the Bendigo-Castlemaine goldfield area feature steeply dipping cleavage in combination with offset laminated quartz veins (Fowler and Winsor, 1996). This conclusion, however,

is in contrast to field observations of chevron folds in the Meguma Group, Nova Scotia by Horne and Culshaw (2000) and to another kinematic model by Bastida et al. (2007). According to the time of quartz vein emplacement (Horne and Culshaw, 2000) and strain pattern analysis (Bastida et al., 2007), both studies observe flexural slip to occur during the late stages of folding, after inter-limb angles of ~60° have been established.

This discrepancy merits further consideration as a recent numerical modeling study by Damasceno et al. (2017) has shown that flexural slip during visco-elastic buckle folding of effective single layer folds is initiated during the early stages of folding. While this observation seems to support the field observations by Fowler and Winsor (1996, 1997), the numerical folds involving flexural slip do not develop chevron fold shapes, but result in sinusoidal, parabolic and box folds (Damasceno et al., 2017). While Damasceno et al. (2017) show that flexural slip initiates in a true multilayer setup (featuring a sinusoidal initial perturbation) for diminishing thickness of the less competent layers (i.e. for a ratio of the less competent layer thickness, s, to the competent layer thickness, h, of s/h=1/8), their results of the flexural slip fold shapes only document their effective single layer setup (i.e. s=0). While it has been shown that true multilayer setups of s/h=1 result in chevron folds (e.g., Ramsay, 1974), the limit of the ratio, s/h for which chevron folds develop, with or without the involvement of flexural slip, has not been quantified and documented in the literature.

This study uses 2D finite element analysis to investigate how the flexural slip mechanism contributes to the development of chevron folds during viscoelastic buckling. Of particular interest is to test whether chevron folds do develop in effective single layer setups as implied by De Sitter (1958), Ramsay (1974), Pollard and Fletcher (2005), and as

observed in several field outcrops (Fowler and Winsor, 1996, 1997; Ryan and Smith, 1998). While Damasceno et al.'s (2017) study seems to contradict these studies and observations, their results are not comprehensive enough to conclude on the importance of the flexural slip mechanism during chevron folding. In order to have a more comprehensive understanding, this study investigates the influence of several model parameters in a series of sensitivity analyses. Of particular interest are the geometry and the wavelength of the initial perturbation, the friction coefficient, the competence contrast, and the overburden thickness.

In addition, for true multilayer setups, the model is benchmarked and compared to plasticine experiments resulting in chevron folds and the ratio of s/h and its influence of slip initiation and the resulting fold shape is documented. This modeling study also analyses the resulting slip distribution (spatial and temporal) of chevron folds, in order to provide an explanation for observations of flexural slip during the later stages of folding (Horne and Culshaw, 2000; Bastida et al., 2007).

2. METHODOLOGY

2.1. GOVERNING EQUATIONS

This study simulates the development of multilayer viscoelastic buckle folds (Mancktelow, 1999; Zhang et al., 2000; Schmalholz et al., 2001; Eckert et al., 2014, 2016; Damasceno et al., 2017) by adopting a linear Maxwell model, which enables the calculation of instantaneous elastic behavior for faster strain rates and time dependent viscous behavior for slower strain rates. Effective stresses are introduced by accounting for pore pressure elements assuming an incompressible fluid and rock grains (i.e. Biot and Willis, 1957; Nur and Byerlee, 1971). This study utilizes 2D plane strain finite element analysis to solve the equations of equilibrium, conservation of mass, constitutive equations, and pore fluid flow via the commercial software package ABAQUS^{TM}. It assumes that the folds extend infinitely and have no displacement along the fold axis direction. As this study follows the same system of governing equations as presented in Eckert et al. (2014), it will not repeat in this paper.

2.2. DOMINANT WAVELENGTH SELECTION

In order to identify the dominant wavelength, λ_{dw}, of the viscoelastic buckle folds, the parameter, R (Schmalholz and Podladchikov, 1999; Schmalholz et al., 2001), is calculated to define whether the folds are developing viscously ($R>1$) or elastically ($R<1$). R is the ratio of the viscous dominant wavelength, λ_{dv}, to the elastic dominant wavelength, λ_{de}. Two general model setups are investigated in this study, effective single layer (the multilayer fold is comprised of layers of equal competence) and true multilayer models

(the multilayer fold is comprised of layers of alternating competence). The dominant wavelengths of the different models are given by Schmalholz and Podladchikov (1999) and Schmalholz et al. (2001) based on Biot's (1965) theory.

For the effective single layer model:

$$R_{eff} = \frac{\lambda_{dv}}{\lambda_{de}} = \sqrt[3]{\frac{\eta_l}{6\eta_m}}\sqrt{\frac{P_o}{G}}$$

For the true multilayer model:

$$R_{multi} = \frac{\lambda_{dv}}{\lambda_{de}} = \sqrt[3]{\frac{N\eta_l}{6\eta_m}}\sqrt{\frac{P_o}{G}}$$

In the above equations, η_l is the viscosity of the competent layers, η_m is the viscosity of the incompetent layers and matrix, G is the shear modulus, N is the number of competent layers, and P_o is the initial layer parallel stress calculated by $P_o = 4\eta_l\dot{\varepsilon}$ (Schmalholz and Podladchikov, 1999), where $\dot{\varepsilon}$ is the constant geologic strain rate.

All models are folded viscously due to values of R smaller than 1 ($R_{eff} = 0.33$ and $R_{multi} = 0.71$). The equations to calculate the respective dominant wavelength are given by:

a) for the effective single layer model:

$$\lambda_{deff} = 2\pi\sqrt[3]{\frac{\eta_l}{6\eta_m}}hN$$

b) for the true multilayer model:

$$\lambda_{dmulti} = 2\pi\sqrt[3]{\frac{N\eta_l}{6\eta_m}}h$$

where h is the thickness of competent layer (Schmid and Podladchikov, 2006). For models employing random white noise, no dominant wavelength is specified.

2.3. MODEL SETUPS

As shown in Figure 2.1, the model is comprised of a central multilayer fold consisting of several sublayers which are separated by frictional interfaces. For the effective single layer setup, there are 10 sublayers and all of the sublayers have the same competence. For the true multilayer setup, in order to maintain the number of competent layers, 10 competent layers and 9 incompetent layers are involved in the model and these sublayers feature alternating magnitudes of competence (Table 2.1). For both setups, the multilayer stack is embedded in a matrix of lower competence (Table 2.1). The thickness of each competent layer is 50 meters. The overburden and basement thickness of the model are set to 1000m. If not specified differently, the material properties (density, viscosity, Young's modulus, Poisson's ratio, and permeability) and model parameters (friction coefficient, strain rate) for the models used are given in Table 2.1 representing the properties of general sedimentary rocks (Schmalholz and Podladchikov, 1999; Jaeger et al., 2007; Damasceno et al., 2017). Both 2D model setups are based on a Maxwell viscoelastic rheology with an initial hydrostatic pore pressure (Mancktelow, 1999; Zhang et al., 2000; Schmalholz et al., 2001; Eckert et al., 2014, 2016; Damasceno et al., 2017). Gravitational pre-stressing is applied to avoid excessive and unrealistic vertical strains due to instantaneous gravitational compaction (Eckert and Connolly, 2007; Smart et al., 2009; Eckert et al., 2014). All models apply 50% of horizontal shortening using a constant geologic strain rate of $10^{-14}\ s^{-1}$ (Twiss and Moores, 2007).

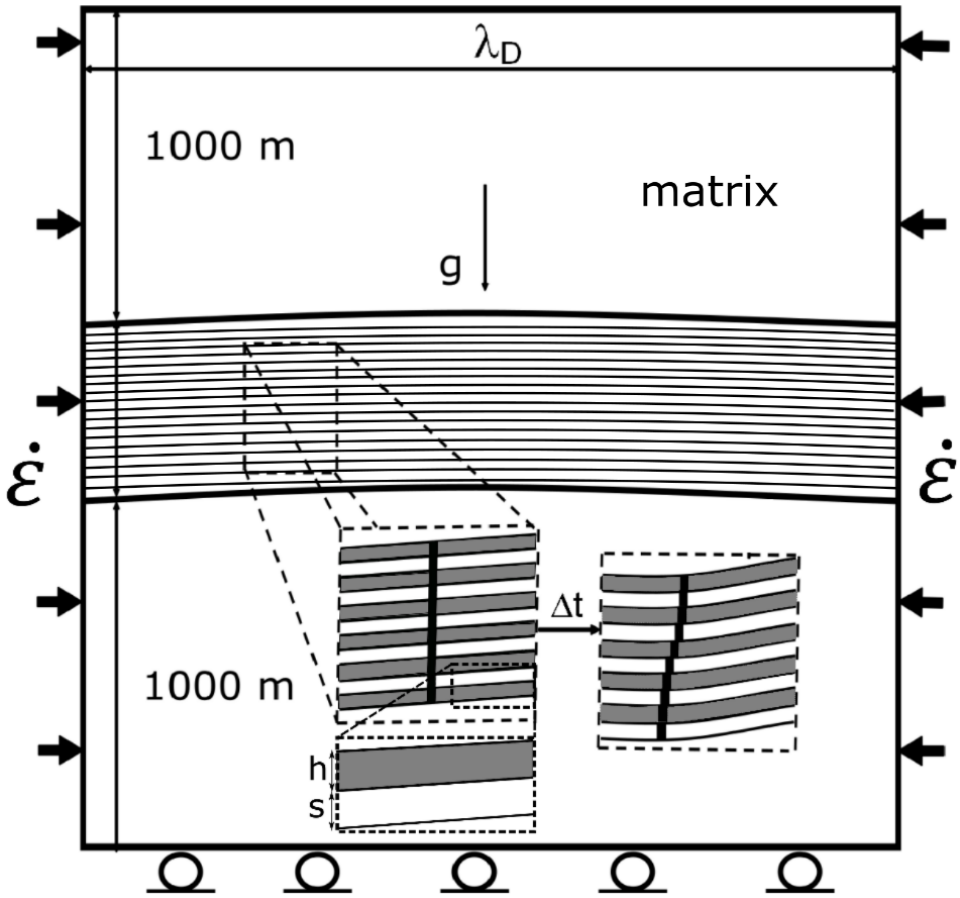

Figure 2.1. Model sketch. Model geometries for the true multilayer (s≠0) and the effective single layer (s=0) cases (after Schmid and Podladchikov, 2006). The model consists of 20 frictional sublayers. Competent layers are represented in gray whereas incompetent layers are in white.

For the following results analyses a series of sensitivity analyses are performed. For the effective single layer setup (Table 2.2), the effects of varying the viscosity contrast of the matrix and the folding layers, wavelength of the initial perturbation, and friction behavior of white noise initial perturbations are applied as the initial wavelength of seed folds.

For the true multilayer setup, sinusoidal, chevron, and white noise initial perturbations with varying values of s/h are simulated to present their influences of the fold geometry and resulting slip distribution (Table 2.3). Table 2.4 shows the influences of the competence contrast of the competent and incompetent folding layers, friction coefficient and overburden load to the slip distribution.

Table 2.1. Material properties for the base model.

Properties	Competent	Incompetent and matrix
Specific gravity (SG)	2.30	2.30
Viscosity (η)	$5.00 \times 10^{21}\ Pa \cdot s$	$5.00 \times 10^{19}\ Pa \cdot s$
Young's Modulus (E)	$30GPa$	$3GPa$
Poisson ratio	0.25	0.25
Permeability (K)	$5.00 \times 10^{-11}\ m^2$	$5.00 \times 10^{-11}\ m^2$
Friction coefficient	0.6	0.6
Strain rate (έ)	$10^{-14}s^{-1}$	$10^{-14}s^{-1}$

Table 2.2. Effective single layer model scenarios considered in this study.

Model setup	Specifications				
	Model #	μ	Viscosity contrast	Overburden load (m)	Initial perturbation
Base model	1	0.6	100	1000	Sinusoidal
	1a	0.4	100	1000	Sinusoidal
	1b	0.2	100	1000	Sinusoidal
	1c	0.6	100	500	Sinusoidal
	1d	0.6	100	2000	Sinusoidal
Viscosity contrast*	2a	0.6	50	1000	Sinusoidal
	2b	0.6	200	1000	Sinusoidal
Initial Perturbation	3a	0.6	100	1000	chevron
	3b	0.6	100	1000	White noise
Friction coefficient (white noise)	3c1	0.4	100	1000	White noise
	3c2	0.2	100	1000	White noise

Table 2.3. True multilayer model scenarios to investigate the influences of initial perturbation geometry and thickness ratio of s/h. All the models use 0.6 as friction coefficient and 1000m as overburden load. The competence contrast is 100.

Model setup	Initial perturbation geometry	s/h
A1	Sinusoidal	1
A2	Sinusoidal	1/2
A3	Sinusoidal	1/4
A4	Sinusoidal	5/4
A5	Sinusoidal	3/2
B1	Chevron	1
B2	Chevron	1/2
B3	Chevron	1/4
B4	Chevron	5/4
B5	Chevron	3/2
C1	White noise	1
C2	White noise	1/2
C3	White noise	1/4
C4	White noise	5/4
C5	White noise	3/2
Turbidite D1*	Sinusoidal	1

*For turbidite model, a permeable material (i.e. sandstone:$k = 5.00 \times 10^{-11} m^2$) and an impermeable material (i.e. shale:$k = 5.00 \times 10^{-19} m^2$) are selected to represent turbidite sequence conditions.

Table 2.4. True multilayer model scenarios to investigate the influences of friction coefficient, overburden load and competence contrast. All the models are applied sinusoidal initial perturbation and s/h equals to 1.

Model setup	Friction coefficient	OVB load	Competence contrast
a	0.6	1000	25
b	0.6	1000	50
c	0.6	1000	200
d	0.2	1000	100
e	0.4	1000	100
f	0.6	500	100
g	0.6	2000	100

3. RESULTS

The results utilize the slip tendency parameter (Morris et al., 1996), Ω, in order to quantify the timing of resulting slip (Appendix A). The relationship between aspect ratio ($aspect\ ratio = \frac{2 \times amplitude}{wavelength}$) and dip angle at the inflection point is used to assess the resulting fold shape and to confirm the development of chevron folds (Ghassemi et al., 2010). The detailed derivation between aspect ratio and dip angle is shown in Appendix B.

3.1. FLEXURAL SLIP FOR EFFECTIVE SINGLE LAYER

The deformed fold profiles and the resulting slip distribution are presented for variations of the friction coefficient, the competence contrast, the geometry of the initial perturbation, and the overburden thickness. As shown by Damasceno et al. (2017) variations in overburden thickness and friction coefficient in an effective single layer setup featuring a sinusoidal initial perturbation do not result in chevron folds. Results from the base model (Models 1, 1a-d) confirm these observations and are shown in Appendix C.

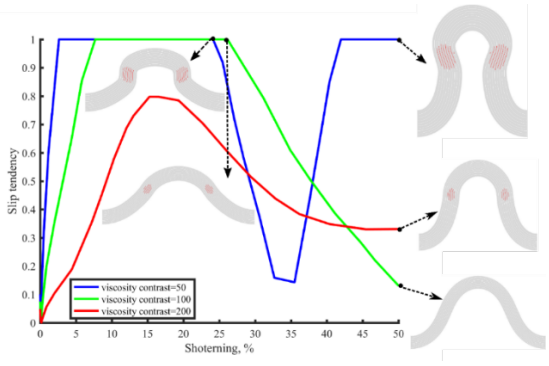

Figure 3.1. Slip tendency evolution based on sinusoidal initial perturbations. Red lines in the fold profiles highlight the location of maximum cumulative slip.

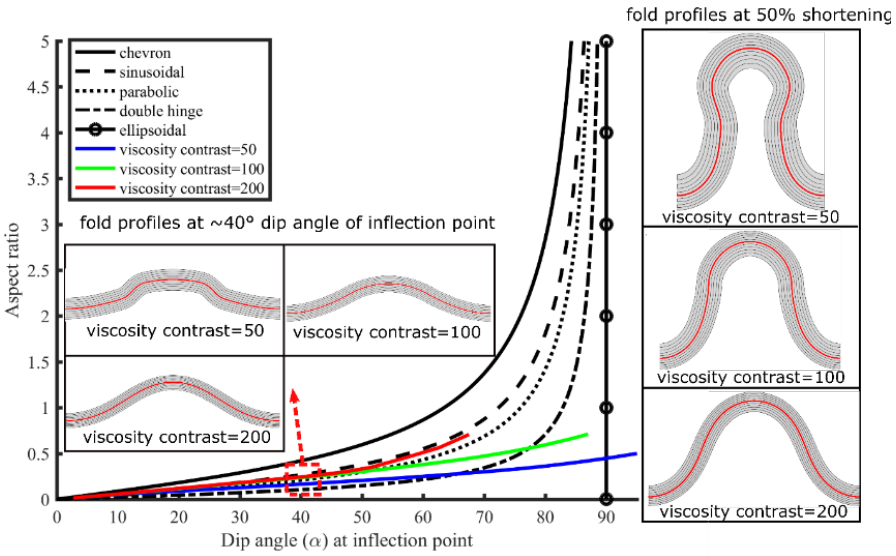

Figure 3.2. The relationship between aspect ratio and dip angle at the inflection point featuring varying viscosity contrasts. Red lines in the fold profiles highlight the location for calculating the aspect ratio.

3.1.1. Viscosity Contrast. Slip evolution and deformed fold profiles for models featuring varying viscosity contrasts of matrix and folding layers (Models 1, 2a, 2b) based on sinusoidal initial perturbations are shown in Figure 3.1. For the low viscosity contrast model (Model 2a; blue line in Figure 3.1), slip initiates during the early stages (~2% shortening), terminates after 25% shortening, and re-initiates during the later stages when the limb overturns. For the mid viscosity contrast model (Model 1; green line), slip initiates at the early stages (~8% shortening) and terminates after 27% shortening. For the high viscosity contrast model (Model 2b; red line), flexural flow dominates and slip is not initiated. For all models, the locations of the maximum cumulative amount of slip are near the inflection points.

It is clear from the final fold shapes shown in Figure 3.1 that chevron folds do not develop as the viscosity ratio varies. For a more detailed analysis of the evolution of fold

geometry, Figure 3.2 shows the aspect ratio with respect to limb dip at the inflection points for both the modeling results and the ideal aspect ratios for chevron, sinusoidal, parabolic, double hinge (box folds), and ellipsoidal fold shapes. The low viscosity contrast model (Model 2a; blue line in Figure 3.2) transforms from the sinusoidal initial perturbation into a double hinge fold from α=10° to α=68°. After α=68° the fold shape develops into an ellipsoidal fold with overturned limbs. The base case model (Model 1; green line in Figure 3.2) transitions from a sinusoidal fold into a parabolic fold until α=55°. From 55°-70° the fold becomes a double hinge fold and then transitions towards an ellipsoidal fold shape. The high viscosity contrast model (Model 2b; red line in Figure 3.2) remains sinusoidal throughout.

3.1.2. Initial Perturbation. Slip evolution and deformed fold profiles for models based on sinusoidal, chevron and white noise initial perturbations (Models 1, 3a, 3b) are shown in Figure 3.3. For the sinusoidal initial perturbation model (Model 1; blue line in Figure 3.3), slip initiates during the early stages (~6% shortening), terminates after 25% shortening. For the chevron initial perturbation model (Model 3a; red line in Figure 3.3), slip initiates at the early stages (~6% shortening) and terminates after 31% shortening. For the white noise initial perturbation model (Model 3b; green line in Figure 3.3), slip initiates at the early stages (~17% shortening) and terminates after 43% shortening. For all models, the locations of the maximum cumulative amount of slip are near the inflection points.

From Figure 3.3, it can be observed that chevron folds do not develop as the initial perturbations varies. For a more detailed analysis of the evolution of fold geometry, Figure 3.4 shows the aspect ratio with respect to limb dip at the inflection points for both the modeling results and the ideal aspect rations for chevron, sinusoidal, parabolic, double

hinge (box folds), and ellipsoidal fold shapes. The sinusoidal initial perturbation model (Model 1; blue line in Figure 3.4) transitions from a sinusoidal fold into a parabolic fold until α=55°. From 55°-70° the fold becomes a double hinge fold and then transitions towards an ellipsoidal fold shape. The chevron initial perturbation model (Model 3a) is separated into top part and bottom part, because the two parts feature different fold geometries. The top part of the chevron initial perturbation model (red dashed line in Figure 3.4) transitions from a sinusoidal fold into a parabolic fold until α=55°. From 55°-77° the fold becomes a double hinge fold and then transitions towards an ellipsoidal fold shape. The bottom part of the chevron initial perturbation model (red dotted line in Figure3.4) remains parabolic throughout.

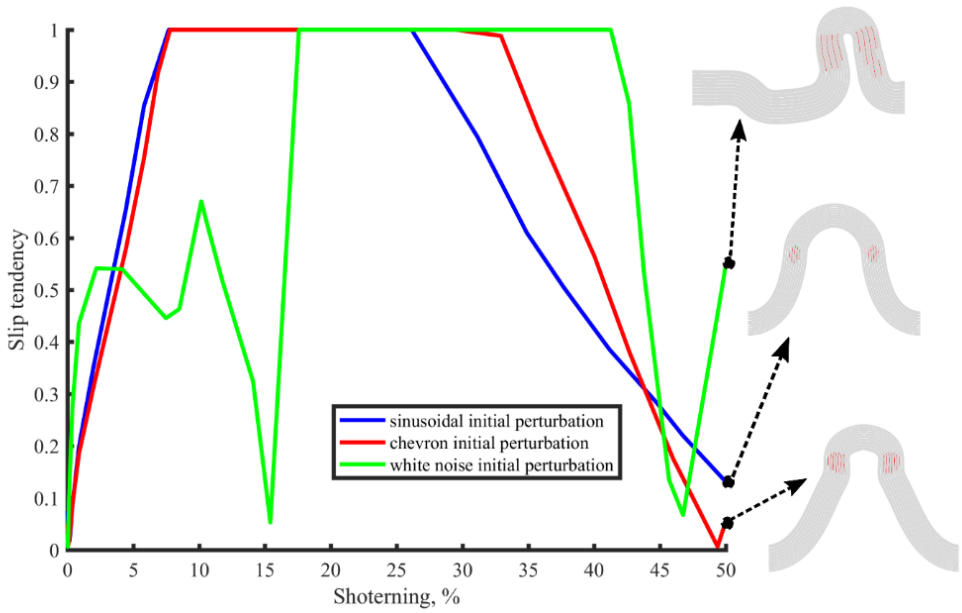

Figure 3.3. Slip tendency evolution featuring sinusoidal, chevron and white noise initial perturbations. Red lines in the fold profiles highlight the location of maximum cumulative slip.

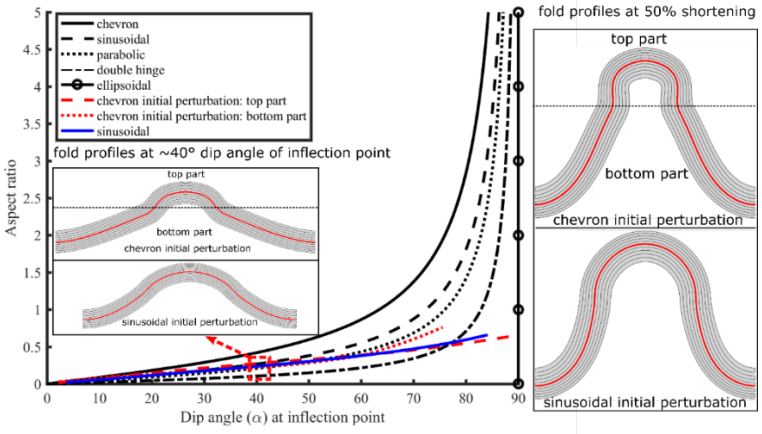

Figure 3.4. The relationship between aspect ratio and dip angle at the inflection point featuring sinusoidal and chevron initial perturbation. Red lines in the fold profiles highlight the location for calculating the aspect ratio.

3.1.3. Friction Coefficient. Slip evolution and deformed fold profiles for models featuring varying friction coefficients of the folding layer interfaces (Models 1, 3c1, 3c2) based on white noise initial perturbations are shown in Figure 3.5. For the high friction coefficient model (Model 1; magenta line in Figure 3.5), slip initiates during the early stages (~7% shortening), terminates after 11% shortening, re-initiates at 17% shortening, then terminates after 20% shortening, and re-initiates at 26% shortening until the end of folding. For the mid friction coefficient model (Model 3c1; red line in Figure 3.5), slip initiates during the early stages (~4% shortening),terminates after 24% shortening, re-initiates at 27% shortening, and terminates after 42% shortening. For the low friction coefficient model (Model 3c2; blue line in Figure 3.5), slip initiates during the early stages (~1% shortening), and terminates after 48% shortening. For all models, the locations of the maximum cumulative amount of slip are near the inflection points.

From Figure 3.5, it can be observed that chevron folds do not develop as the friction coefficient varies based on white noise initial perturbations. Because deformed fold

profiles based on white noise initial perturbations are complicated (i.e. asymmetric, multiple wavelengths), only the aspect ratio of the resulting dominant wavelength are shown in Figure 3.6 (highlighted by red lines in the fold profiles. The high friction coefficient model (Model 1; magenta line in Figure 3.6) remains sinusoidal until α=50°, transforms to parabolic from α=50° to α=60°, to double hinge from α=60° to α=75°, before reaching ellipsoidal shape until α=90°. The mid friction coefficient model (Model 3c1; red line in Figure 3.6) transitions from a sinusoidal fold into a double hinge fold until α=72°. After α=72° the fold transitions towards an ellipsoidal fold shape. The low friction coefficient model (Model 3c2; blue line in Figure 3.6) transforms from the sinusoidal perturbation into a double hinge fold from α=10° to α=77°. After α=77° the fold shape develops into an ellipsoidal fold.

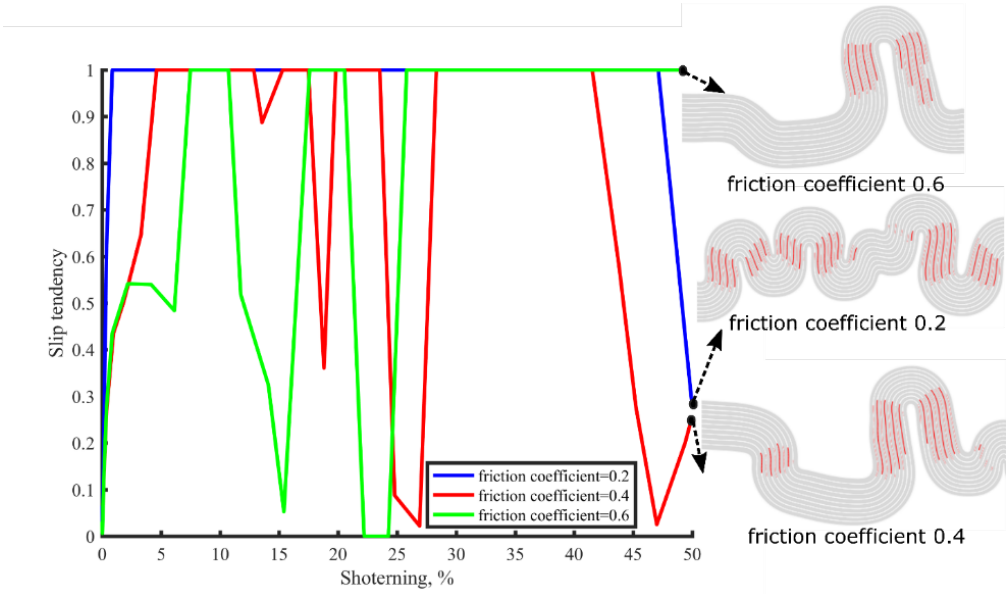

Figure 3.5. Slip tendency evolution featuring varying friction coefficients based on white noise initial perturbations. Red lines in the fold profiles highlight the location of maximum cumulative slip.

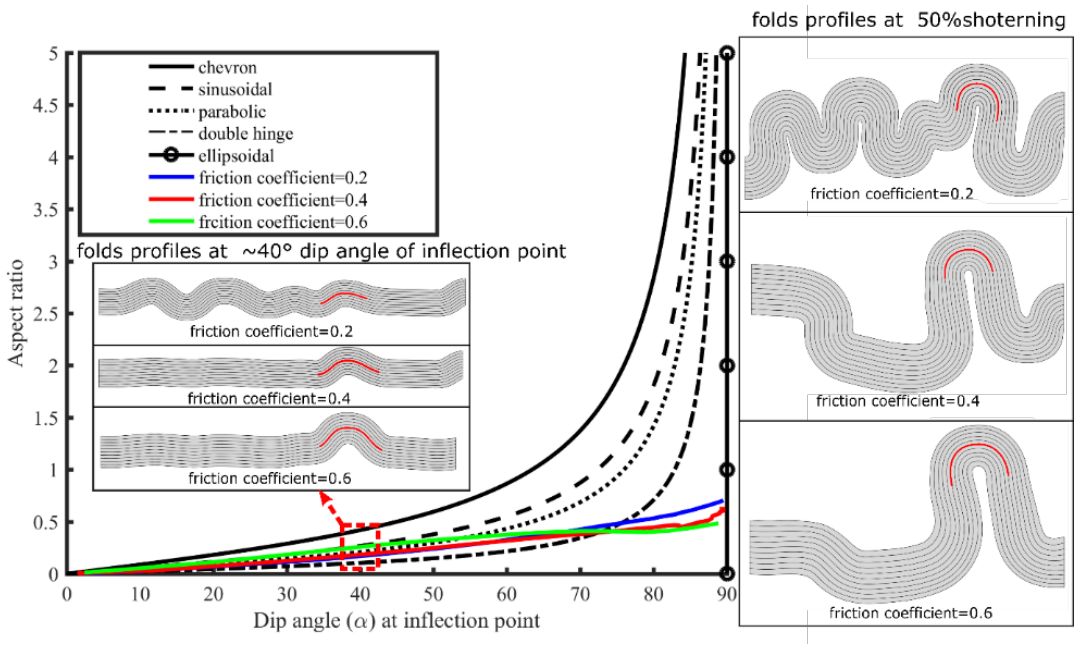

Figure 3.6. The relationship between aspect ratio and dip angle at the inflection point featuring varying friction coefficient based on white noise initial perturbations. Red lines in the fold profiles highlight the location for calculating the aspect ratio for the resulting dominant wavelength.

3.2. FLEXURAL SLIP FOR TRUE MULTILAYER

The deformed fold profiles and the resulting slip distribution are presented for variations of the friction coefficient, overburden thickness, the competence contrast, the geometry of the initial perturbation, and the ratio of incompetent to competent layer thickness. The results utilize the slip tendency parameter (Morris et al., 1996), Ω, in order to quantify the timing of resulting slip (Appendix A). The relationship between aspect ratio ($aspect\ ratio = \frac{2 \times amplitude}{wavelength}$) and dip angle at the inflection point is used to assess the resulting fold shape and to confirm the development of chevron folds (Ghassemi et al.,

2010). The detailed derivation between aspect ratio and dip angle is shown in Appendix B. The deformed fold profiles and the resulting slip distribution are presented.

3.2.1. Varying s/h for Sinusoidal, Chevron and White Noise Initial Perturbations. This sections investigates the influence of the ratio of incompetent to competent layer thickness, s/h, for different initial perturbation geometries. For sinusoidal initial perturbations (Models A1-A5; Table 4.1), Figure 3.7.1a shows the resulting fold profiles after 50% shortening and the location of the associated maximum cumulative slip (red lines). It can be observed that chevron shapes develop at 50% for all investigated ratios of s/h; however only models of s/h=1, 0.5, and 0.25 involve the initiation of flexural slip. Slip is initiated on the upper part of the competent layer near the hinge zone; the lower s/h, the more surfaces initiate slip. The slip evolution (Figure 3.7b) shows that for Models A2 and A3 (s/h=0.5 and 0.25; green and red line in Figure 3.7b), slip initiates during a short period of deformation, i.e. between ~33% and ~35% of shortening. For Model A1 (s/h=1; blue line) slip initiates between ~28% and ~42% of shortening. For Models A4 and A5; cyan and magenta lines), flexural flow dominates and slip is not initiated.

For a more detailed analysis of the evolution of fold geometry, Figure 3.8a shows the aspect ratio with respect to limb dip at the inflection points. For lower s/h, chevron folds result at higher limb dip angles. In summary, all models transform from sinusoidal folds to chevron folds with hinge collapses at varying degrees of the resulting limb dip angle (i.e. the model of s/h=0.25, 0.5, 1, 1.25, 1.5 transform from sinusoidal perturbations to chevron folds at α=70°, 63°, 49°, 45°, 42° respectively). Figure 3.8b illustrates the slip initiations and terminations of varying s/h models based on sinusoidal initial perturbations. Star and polygon signals highlight slip initiations and slip terminations respectively. The

model of s/h=0.25 (red line), slip initiates from α=70° to 72° and the aspect ratio increases rapidly. The model of s/h=0.5 (green line), slip initiates at α=63° and α remains constant until the termination of slip. The model of s/h=1 (blue line), slip initiates from α=53° to 57°. It can be observed that for all flexural slip models (Model A1, A2, and A3; blue, green and red lines), when the slip initiates, the models start to transform from sinusoidal perturbations to chevron folds and the transition speeds are faster than flexural flow folds (Model A4 and A5; cyan and magenta lines).

For chevron initial perturbations (Models B1-B5; Table 4.1), Figure 3.7a shows the resulting fold profiles after 50% shortening and the location of the associated maximum cumulative slip (red lines). It can be observed that chevron shapes develop at 50% for all investigated ratios of s/h; however only models of s/h=1, 0.5, and 0.25 involve the initiation of flexural slip. Slip is initiated on the upper part of the competent layer near the hinge zone. The slip evolution (Figure 3.9b) shows that for Models B2 and B3 (s/h=0.5 and 0.25; green and red line in Figure 3.9b), slip initiates during a short period of deformation, i.e. the model of s/h=0.25, slip initiates at ~33% of shortening and terminates immediately, and the model of s/h=0.5, slip initiates between ~32% to 35% of shortening. For Model A1 (s/h=1; blue line) slip initiates between ~28% and ~38% of shortening. For Models A4 and A5; cyan and magenta lines), flexural flow dominates and slip is not initiated.

For a more detailed analysis of the evolution of fold geometry, Figure 3.10a shows the aspect ratio with respect to limb dip at the inflection points. For lower s/h, chevron folds result at higher limb dip angles. In summary, all models transform from sinusoidal to chevron folds at α=68°, 61°, 42°, 38°, 34° respectively). Figure 3.10b illustrates the slip

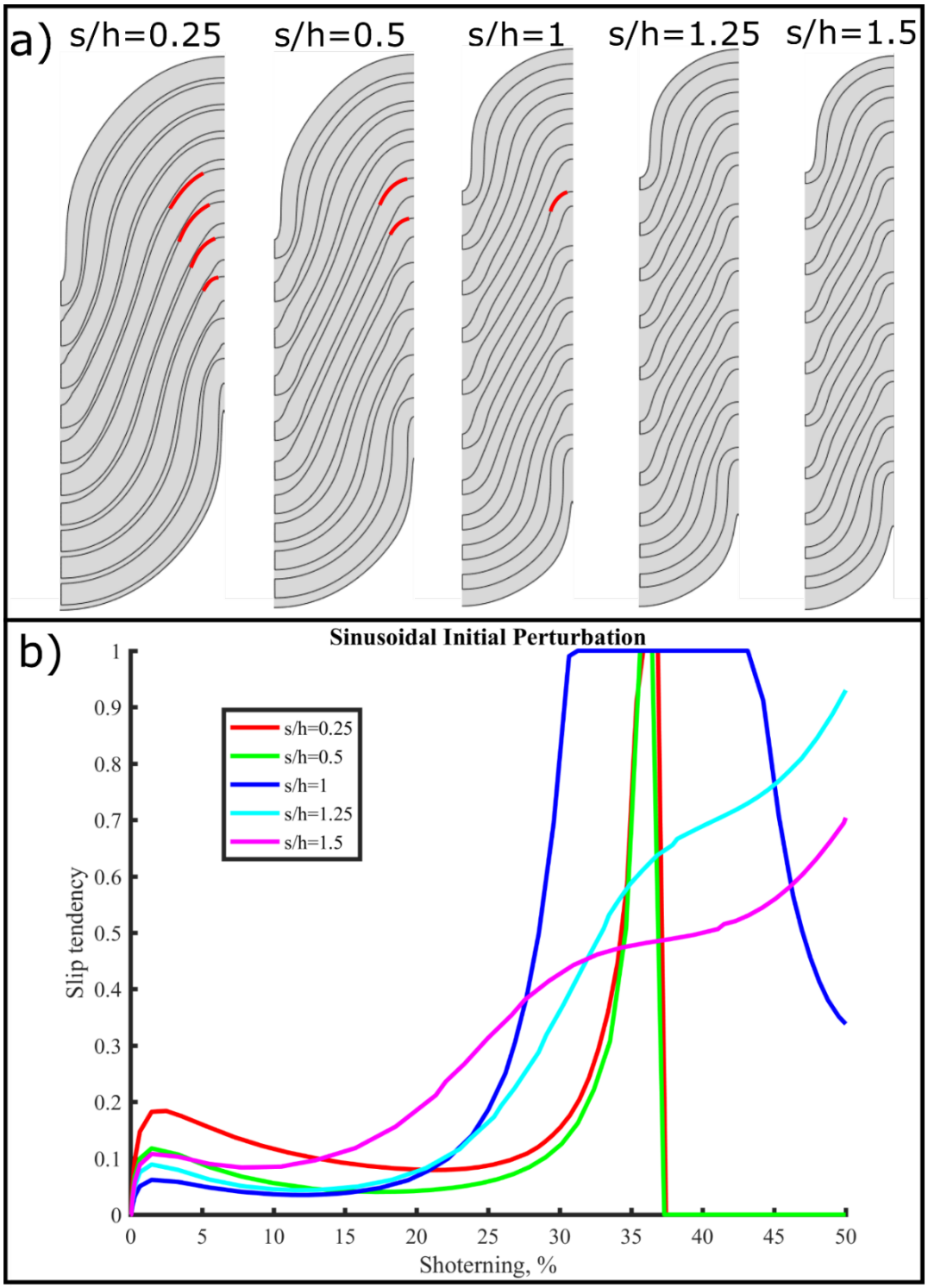

Figure 3.7. Slip evolution based on sinusoidal initial perturbations. a) Fold profiles of the true multilayer models featuring varying s/h values based on sinusoidal initial perturbations. Red lines in the fold profiles highlight the location of maximum cumulative slip. b) Slip tendency evolution with respect to shortening.

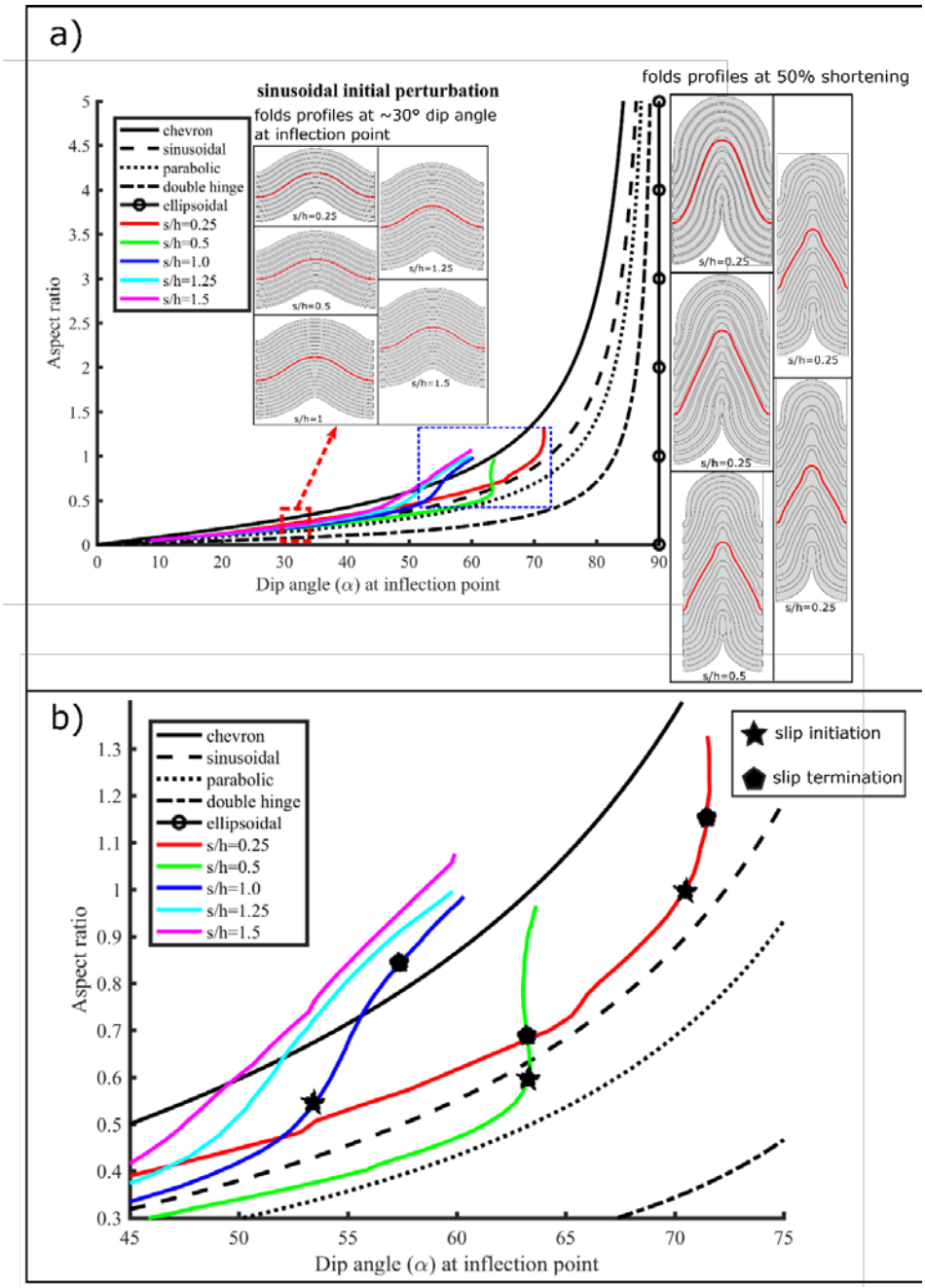

Figure 3.8. Fold shape evolution based on sinusoidal initial perturbations. a) The relationship between aspect ratio and dip angle at the inflection point featuring varying s/h value based on sinusoidal initial perturbations for both the modeling results and the ideal chevron, sinusoidal, parabolic, double hinge and ellipsoidal fold shapes. Red lines in the fold profiles highlight the location of calculating aspect ratio. b) At the end of folding (blue dashed rectangle in Figure 3.8a), the relationship between aspect ratio and dip angle at the inflection points. It is of note that star and polygon signals highlight slip initiations and terminations respectively.

initiations and terminations of varying s/h models based on chevron initial perturbations. Star and polygon signals highlight slip initiations and slip terminations respectively. The model of s/h=0.25 (red line), slip initiates from α=68° to 69°. The model of s/h=0.5 (green line), slip initiates from α=61° to α=62°. The model of s/h=1 (blue line), slip initiates from α=52° to 54°. It can be observed that for all flexural slip models (Model B1, B2, and B3; blue, green and red lines), when the slip initiates, the models start to transform from sinusoidal perturbations to chevron folds and the transition speeds are faster than flexural flow folds (Model A4 and A5; cyan and magenta lines). For white noise initial perturbations (Models C1-C5; Table 4.1), Figure 3.11a shows the resulting fold profiles after 50% shortening and the location of the associated maximum cumulative slip (red lines). It can be observed that chevron shapes develop at 50% for all investigated ratios of s/h; however only models of s/h=1, 0.5, and 0.25 involve the initiation of flexural slip. Slip is initiated on the upper part of the competent layer near the hinge zone. It can be observed that different dominant wavelength generated by less s/h model (Model C3: s/h=0.25). The slip evolution (Figure 3.11b) shows that for Models C2 and C3 (s/h=0.5 and 0.25; green and red line in Figure 3.11b), slip initiates during the earlier stages (~5% shortening for s/h=0.25 and ~6% shortening for s/h-0.5), terminates immediately (~5.2% shortening for s/h=0.25 and ~11% shortening for s/h=0.5) and re-initiates during the later stages (~35% shortening for s/h=0.25 and ~23% shortening for s/h=0.5). For the mid s/h value model (Model C1; blue line in Figure 3.11), slip initiates at the earlier stages (~9% shortening) and terminates after 17% shortening. For the high s/h value models (Model C4, C5; cyan line and magenta line in Figure 3.11), flexural flow dominates and slip is not initiated. For

all models, the locations of the maximum cumulative amount of slip are near the hinge zones.

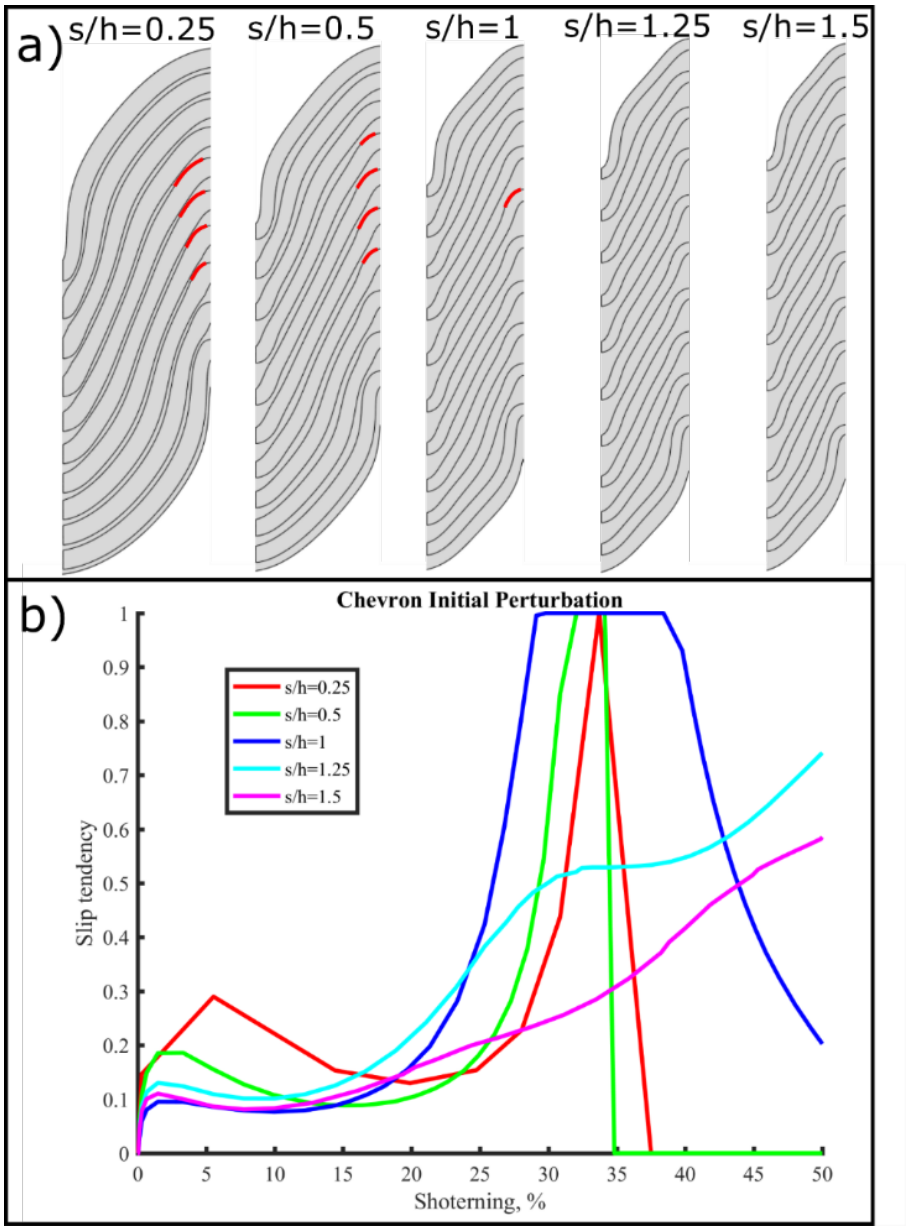

Figure 3.9. Fold profiles and slip tendency of the true multilayer models featuring varying s/h values based on chevron initial perturbations. Red lines in the fold profiles highlight the location of maximum cumulative slip.

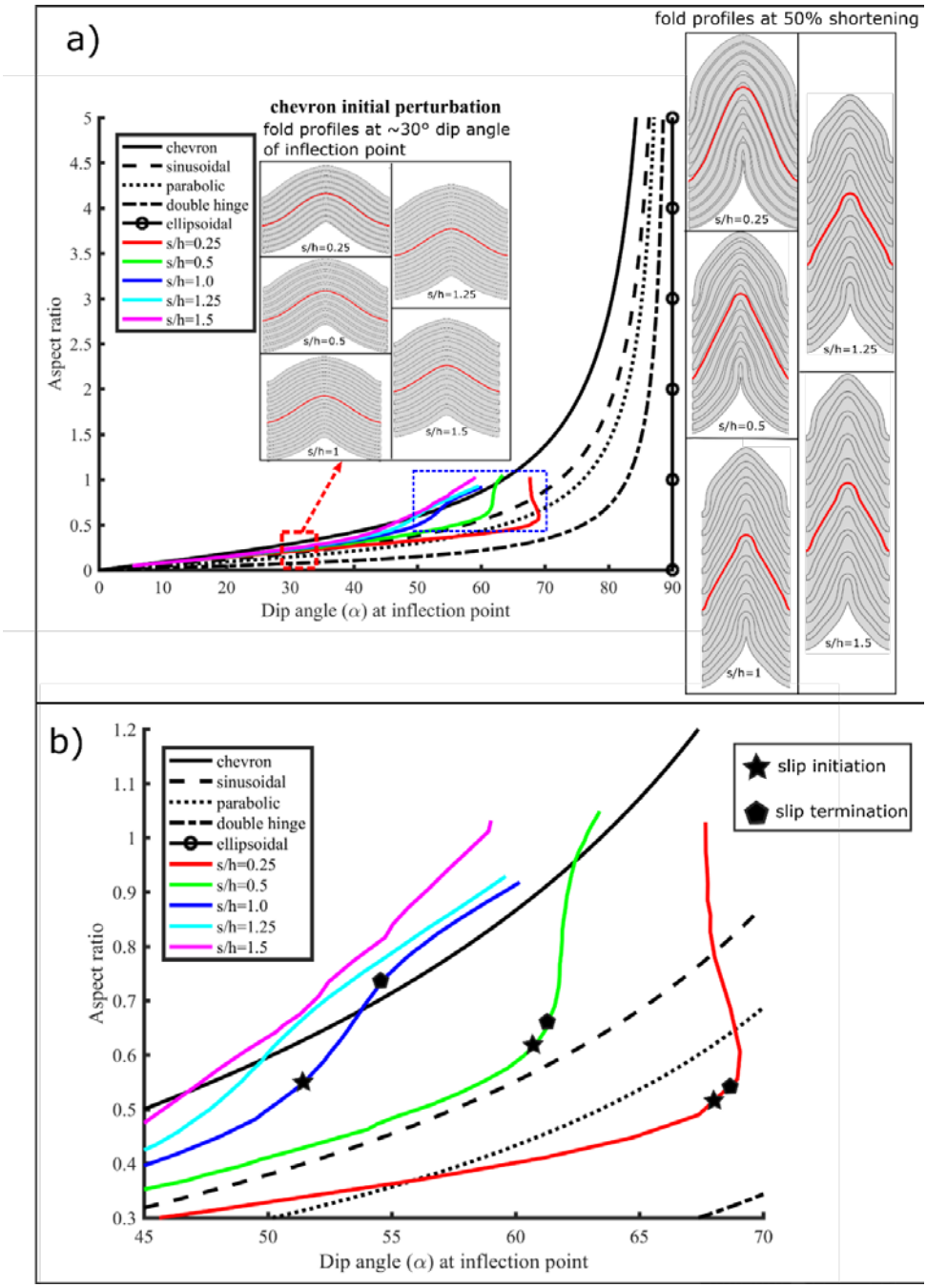

Figure 3.10. Fold shape evolution based on chevron initial perturbations. a) The relationship between aspect ratio and dip angle at the inflection point featuring varying s/h value based on chevron initial perturbations for both the modeling results and the ideal chevron, sinusoidal, parabolic, double hinge and ellipsoidal fold shapes. Red lines in the fold profiles highlight the location of calculating aspect ratio. b) At the end of folding (blue dashed rectangle in Figure 3.10a), the relationship between aspect ratio and dip angle at the inflection points. It is of note that star and polygon signals highlight slip initiations and terminations respectively.

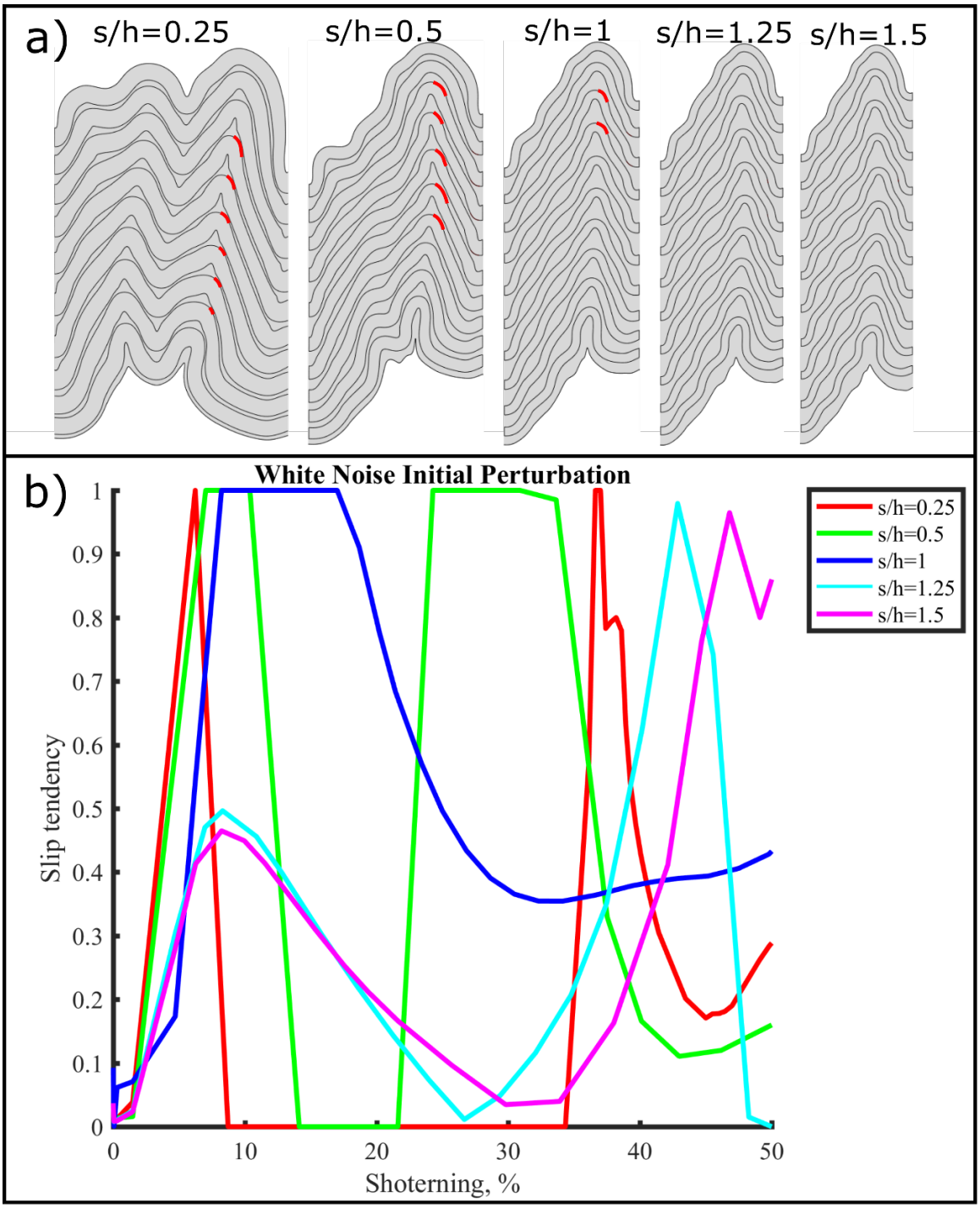

Figure 3.11. Fold profiles and slip tendency of the true multilayer models featuring varying s/h values based on white noise initial perturbations. Red lines in the fold profiles highlight the location of maximum cumulative slip.

3.2.2. Competence Contrast. Slip evolution for models featuring varying competence contrasts between competent and incompetent folding layers (Models A1, a, b, c) based on sinusoidal initial perturbations are shown in Figure 3.12. For low competence contrast models (Model a, b; blue line and green line in Figure 3.12), slip initiates during the later stages (~24% shortening when competence contrast is 25 and ~25% shortening when competence contrast is 50), and terminates at ~ 45% shortening for both two models. For the mid competence contrast model (Model A1; magenta line in Figure 3.12), slip initiates at the later stages (~30% shortening) and terminates after 42% shortening. For the high competence contrast model (Model c; red line in Figure 3.12), flexural flow dominates and slip is not initiated.

From Figure 3.12, it shows that in the lower competence contrast model, slip initiates earlier and terminates later. For a more detailed analysis of the evolution of fold geometry, Figure 3.13 shows the aspect ratio with respect to limb dip at the inflection points for both the modeling results and the ideal aspect rations for chevron, sinusoidal, parabolic, double hinge (box folds), and ellipsoidal fold shapes. The model with competence contrast is 25 (Model a; blue line in Figure 3.13) remains the sinusoidal fold shape from α=10° to α=44°. After α=44° the folds transforms from the sinusoidal perturbation into a chevron fold with hinge collapse. The model with competence contrast is 50 (Model b; green line in Figure 3.13) transforms from the sinusoidal perturbation into a chevron fold with hinge collapse at α=45°. The model with competence contrast is 100 (Model A1; magenta line in Figure 3.13) transforms from the sinusoidal perturbation into a chevron fold with hinge collapse at α=46°. The model with competence contrast is 200 (Model c; red line in Figure

3.12) transitions from the sinusoidal perturbation into a chevron fold with hinge collapse at α=47°.

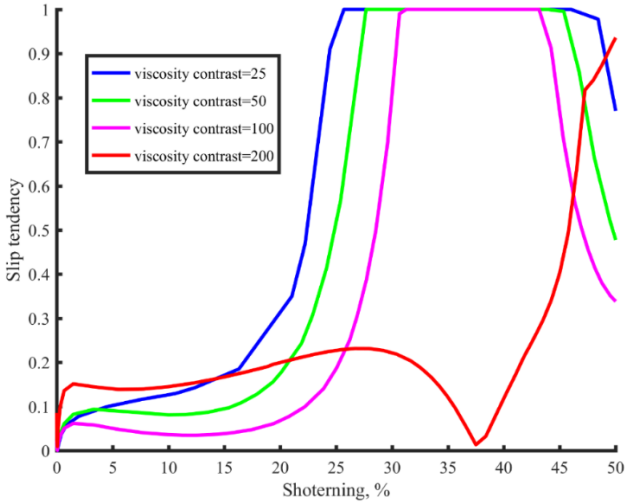

Figure 3.12. Slip tendency of the true multilayer models featuring varying competence contrasts between competent and incompetent folding layers. Except for viscosity contrast, the other material properties are equal to model A1.

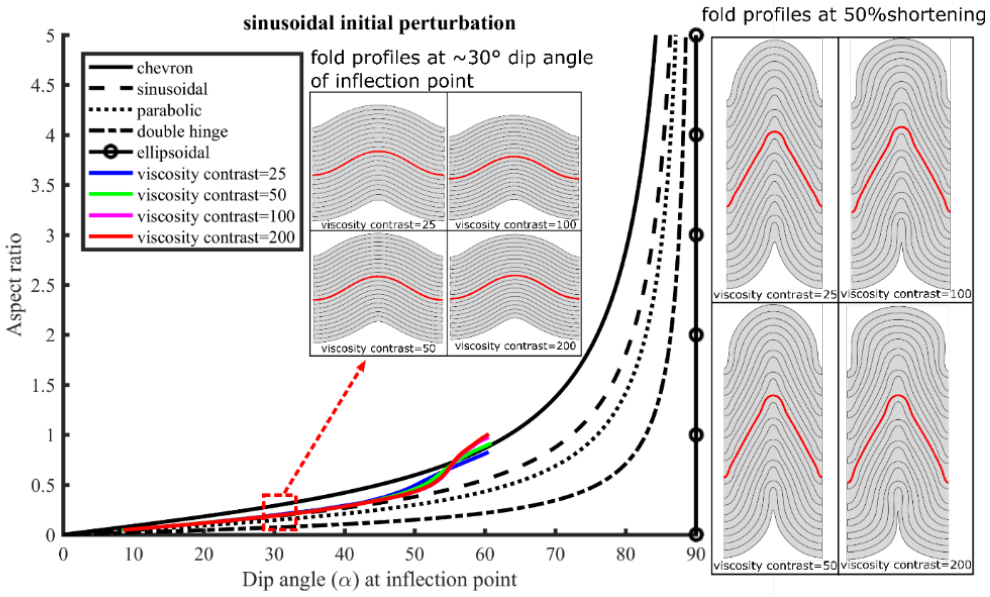

Figure 3.13. The relationship between aspect ratio and dip angle at the inflection point featuring varying competence contrasts. Red lines in the fold profiles highlight the location of calculating aspect ratio.

3.2.3. Friction Coefficient. Slip evolution for models featuring varying the friction coefficients of the folding layer interfaces (Models A1, d, e) based on sinusoidal initial perturbations are shown in Figure 3.14. For the lubricated model (Model d; blue line in Figure 3.14), slip initiates during the later stages (~24% shortening). For the less lubricated model (Model e; magenta line in Figure 3.14), slip initiates at the later stages (~27% shortening) and terminates after 44% shortening. For the coarse model (Model A1; red line in Figure 3.14), slip initiates at the later stages (~28% shortening) and terminates after 43% shortening

From Figure 3.14, it shows that in the lower friction coefficient model, slip initiates earlier and terminates later. For a more detailed analysis of the evolution of fold geometry, Figure 3.15 shows the aspect ratio with respect to limb dip at the inflection points for both the modeling results and the ideal aspect rations for chevron, sinusoidal, parabolic, double hinge (box folds), and ellipsoidal fold shapes. All models transform from sinusoidal perturbations into chevron folds with hinges collapse at α=45°.

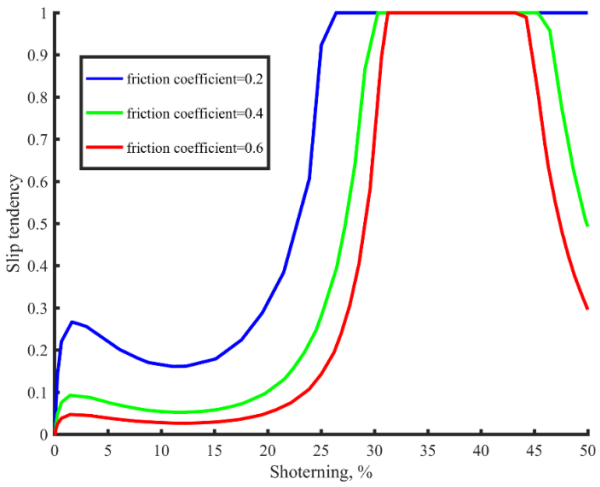

Figure 3.14. Slip tendency of the true multilayer models featuring varying friction coefficients based on sinusoidal initial perturbations.

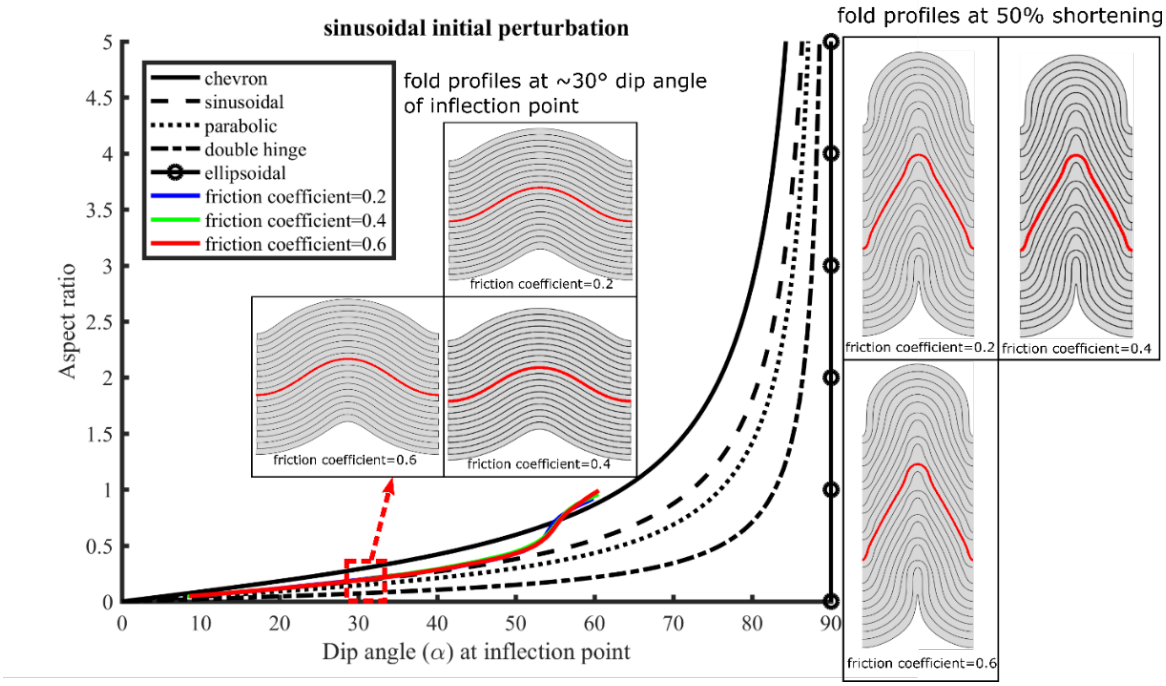

Figure 3.15. The relationship between aspect ratio and dip angle at the inflection point featuring varying friction coefficients based on sinusoidal initial perturbations. Red lines in the fold profiles highlight the location of calculating aspect ratio.

3.2.4. Overburden Load. Slip evolution for models featuring varying overburden loads (Models A1, f, g) based on sinusoidal initial perturbations are shown in Figure 3.16. For the low overburden load model (Model f; blue line in Figure 3.16), slip initiates during the later stages (~22% shortening), terminates after ~25% shortening and then re-initiates at ~38% shortening until ~45% shortening. For the mid overburden load model (Model A1; magenta line in Figure 3.16), slip initiates at the later stages (~30% shortening) and terminates after 45% shortening. For the large overburden load model (Model g; red line in Figure 3.16), flexural flow dominates and slip is not initiated.

From Figure 3.16, it shows that in the overburden affects the slip evolution of chevron folding. For a more detailed analysis of the evolution of fold geometry, Figure

3.16 shows the aspect ratio with respect to limb dip at the inflection points for both the modeling results and the ideal aspect rations for chevron, sinusoidal, parabolic, double hinge (box folds), and ellipsoidal fold shapes. All models transform from sinusoidal perturbations into chevron folds with hinges collapse at α=45°. The overburden load does not affect the evolution of fold geometry.

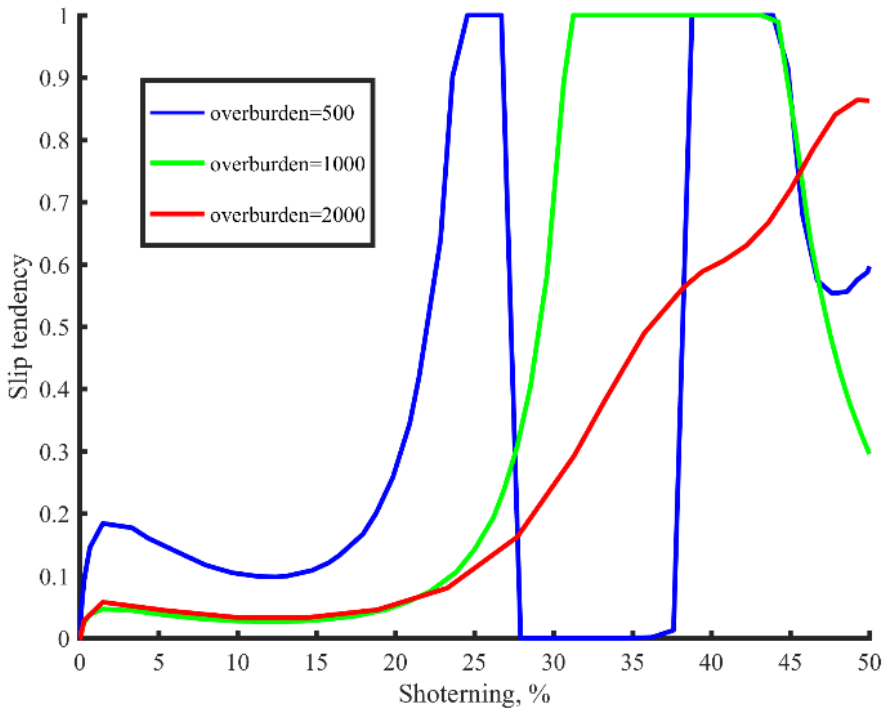

Figure 3.16. Slip tendency of the true multilayer models featuring varying overburden loads based on sinusoidal initial perturbations.

4. DISCUSSION

The numerical modeling results presented reveal a more quantitative understanding of the role of the flexural slip process during the development of chevron folds. This section discusses: (a) the non-development of chevron folds in effective single-layer folds, (b) chevron folds in multilayer folds, with comparisons of the numerical modeling results to laboratory experiments and field observations, and (c) the relative importance of key parameters during the development of chevron folds.

4.1. EFFECTIVE SINGLE LAYER SETUPS

The kinematic models of De Sitter (1964) and Pollard and Fletcher (2005) are based on initial chevron perturbations and predict slip to initiate early during amplification of chevron folds. The early onset of slip has also been observed in numerical models of effective single layer buckle folds based on sinusoidal initial perturbation by Damasceno et al. (2017). However, while their results show that flexural slip in effective single layer buckle folds significantly affects fold shape, chevron folds based on sinusoidal initial perturbations do not develop. To account for the differences of the initial perturbations, this study extends Damasceno et al.'s (2017) study by investigating initial sinusoidal, chevron, and random white noise perturbations. In addition, the effects of viscosity contrast, and friction coefficient (based on white noise initial perturbations) are shown. The results presented confirm Damasceno et al.'s (2017) study: chevron folds do not develop for all variations of initial perturbation, viscosity contrast and friction coefficient considered. The results confirm that flexural slip in effective single layer setups initiates

during the early stages of folding (Table 4.1). They are also in agreement with the conceptual flexural slip model by Tanner (1989) where slip values increase towards the inflection points in the limbs. With respect to the resulting fold shapes, the results presented suggest that flexural slip favors the development of box folds in effective single layer setups. While it has been observed and suggested that box folds develop in anisotropic multilayer systems (e.g. Johnson and Honea, 1976; Price and Cosgrove, 1990; Fowler and Winsor, 1996), the presence of flexural slip in effective single layer box folds, to the authors' knowledge, has not been documented in analogue models and field observations, and thus merits further investigations.

It is also interesting to note that, based on white noise initial perturbations, lower friction coefficient models result in amplified wavelengths shorter than the dominant wavelength as predicted by Schmalholz and Podladchikov, 1999 and by Schmalholz et al., 2001. The relationship between the friction coefficient and dominant wavelength merits further evaluation and is beyond of the scope of this paper. However, while their results show that flexural slip in effective single layer buckle folds significantly affects fold shape, chevron folds based on sinusoidal initial perturbations do not develop. To account for the differences of the initial perturbations, this study extends Damasceno et al.'s (2017) study by investigating initial sinusoidal, chevron, and random white noise perturbations. In addition, the effects of viscosity contrast, and friction coefficient (based on white noise initial perturbations) are shown. The results presented confirm Damasceno et al.'s (2017) study: chevron folds do not develop for all variations of initial perturbation, viscosity contrast and friction coefficient considered.

Table 4.1. The results of true multilayer and effective single layer model scenarios to investigate the influences of initial perturbation and varying the value of s/h.

Model setup	Fold profile	Stage of slip initiation
1	Symmetric ellipsoidal folds	Early stages
A1	Symmetric chevron folds	Later stages
A2	Symmetric chevron folds	Later stages
A3	Symmetric chevron folds	Later stages
A4	Symmetric chevron folds	No slip
A5	Symmetric chevron folds	No slip
3a	Symmetric combination folds	Early stages
B1	Symmetric chevron folds	Later stages
B2	Symmetric chevron folds	Later stages
B3	Symmetric chevron folds	Later stages
B4	Symmetric chevron folds	No slip
B5	Symmetric chevron folds	No slip
3b	Asymmetric folds	Early stages
C1	Asymmetric chevron folds	Early stages
C2	Asymmetric chevron folds	Early stages, re-initiates at the later stages
C3	Asymmetric chevron folds	Early stages, re-initiates at the later stages
C4	Asymmetric chevron folds	No slip
C5	Asymmetric chevron folds	No slip

4.2. TRUE MULTILAYER SETUPS

Price and Cosgrove (1990) state that chevron folds develop by buckling of multilayers with alternating competence. The observations of Horne and Culshaw (2001) and Fowler and Winsor (1996, 1997) suggest that flexural slip is an important mechanism during the development of chevron folds based on true multilayer setups. The results in this study are partly in agreement with Tanner (1989) that lower fractions of incompetence thickness with respect to the flexural slip mechanism occur during development of chevron

folds. However, there is an exception that when fractions of incompetence thickness equals to zero (effective single layer), no chevron folds develop.

In order to investigate the evolution of fold profiles in the development of chevron folds, plasticine analog models suggest that chevron folds evolve from sinusoidal or double hinged folds (Ghosh, 1968; Dubey and Cobbold, 1977; Behzadi and Dubey, 1980; Fowler and Winsor, 1996). Damasceno et al. (2017) also evaluate changing fold profiles, and the resulting folds develop sinusoidal to non-chevron folds. Table 4.2 documents the evolution of fold profiles, showing whether there are sinusoidal or chevron initial perturbations, chevron folds in true multilayer setups develop from sinusoidal seed folds, and in some cases (i.e. s/h=0.5, based on sinusoidal initial perturbations; s/h=1, based on chevron initial perturbations) transform to parabolic before becoming chevron.

Analog laboratory experiments suggest slip initiates during the early stages, the rate of slip is slow, then increases rapidly during later stages and terminates before folds lock up (Behzadi and Dubey, 1980). However, field observations show that slip initiates during later stages (Horne and Culshaw, 2001). These are in the contrast of Damasceno et al. (2017)'s results that slip initiates during the early stages and no chevron folds developing by observations of the slip tendency parameter. Our study verifies that slip in chevron folds are different with the other buckle folds in true multilayer setups. It is initiates during the later stages based on sinusoidal and chevron initial perturbations or re-initiates at late when white noise is applied as initial perturbations (Table 4.1). For sinusoidal and chevron initial perturbation setups, slip terminates before the folds lock up. However, there is one exception when the fraction of competence thickness is high (i.e. s/h=1), there is no observed folding lock up stages. It is difficult to determine the relationship between slip

termination and folding lock up. Field observations also show the folds lock up around inter-limb angle of 60°. This phenomenon is observed in Figures 3.6 and 3.7 where there is a sharp transition of fold shape after slip is initiated**.**

Moreover, field observations show that in true multilayer setups, the location of maximum cumulative slip is near the hinge zone based on the thickness of veins (Fowler and Winsor, 1997; Horne and Culshaw, 2001). This is in contrast with analog laboratory model that cumulative slip is similar on fold limbs and hinge zones. Our models confirm that the location of maximum cumulative slip is near the hinge zones.

Table 4.2. The evolution of fold profiles in the development of chevron folds at sinusoidal and chevron initial perturbations and varying the s/h conditions based on true multilayer setups. Initial seed fold type is underlined.

Model setup	Fold profile
A1	Sinusoidal folds → <u>sinusoidal folds</u> → chevron folds
A2	Sinusoidal folds → <u>sinusoidal folds</u> → parabolic → chevron folds
A3	Sinusoidal folds → <u>sinusoidal folds</u> → chevron folds
A4	Sinusoidal folds → <u>sinusoidal folds</u> → chevron folds
A5	Sinusoidal folds → <u>sinusoidal folds</u> → chevron folds
B1	Chevron folds → <u>sinusoidal folds</u> → parabolic folds → sinusoidal folds → chevron folds
B2	Chevron folds → <u>sinusoidal folds</u> →chevron folds
B3	Chevron folds → <u>sinusoidal folds</u> →chevron folds
B4	Chevron folds → <u>sinusoidal folds</u> →chevron folds
B5	Chevron folds → <u>sinusoidal folds</u> →chevron folds

4.3. POSSIBLE ALTERNATING INFLUENCES

Several field results (Fowler and Winsor, 1996, 1997; Horne and Culshaw, 2001) show that chevron folds develop in turbidite sequence conditions (alternating permeability

and competence). In addition, this study proposes a new aspect of folding, variation in initial wavelength. These two parameters significantly affect the geometries of resulting folds. In this section, more extensions of turbidite setups and varying initial wavelength based on effective single layer setups are discussed.

4.3.1. Turbidite Setups. The properties of turbidite setups are shown in Table 2.3 (Model turbidite D1). To make the model realistic, the thickness of folding layers is reduced to 50 cm and the dominant wavelength is decreased as well with respect to the thinner layer thickness. From literatures, turbidites not only represent mechanical multilayer, but also have permeable contrast to result overpressure (Eckert et al., 2015). The results of slip evolution are in agreement with the initiation of slip is earlier than base model, because overpressure results the reactivation of slip. Moreover, the fold profiles vary along the hinge line: parabolic at culmination, chevron at middle, and concentric folds at terminations (e.g. Figure 4.1). This is quite similar to the plasticine analog models from Fowler and Winsor (1996) who design their model according to geological settings involving viscosity contrasts and turbidite sequences. They also observe the changes in fold profiles, but differ from this study: box folds at culmination, chevron shaped at middle, and mitre folds at terminations (e.g. Figure 4.2).

Moreover, field observations show that in true multilayer setups, the location of maximum cumulative slip is near the hinge zone based on the thickness of veins (Fowler and Winsor, 1997; Horne and Culshaw, 2001). This is in contrast with analog laboratory model that cumulative slip is similar on fold limbs and hinge zones. Our models confirm that the location of maximum cumulative slip is near the hinge zones.

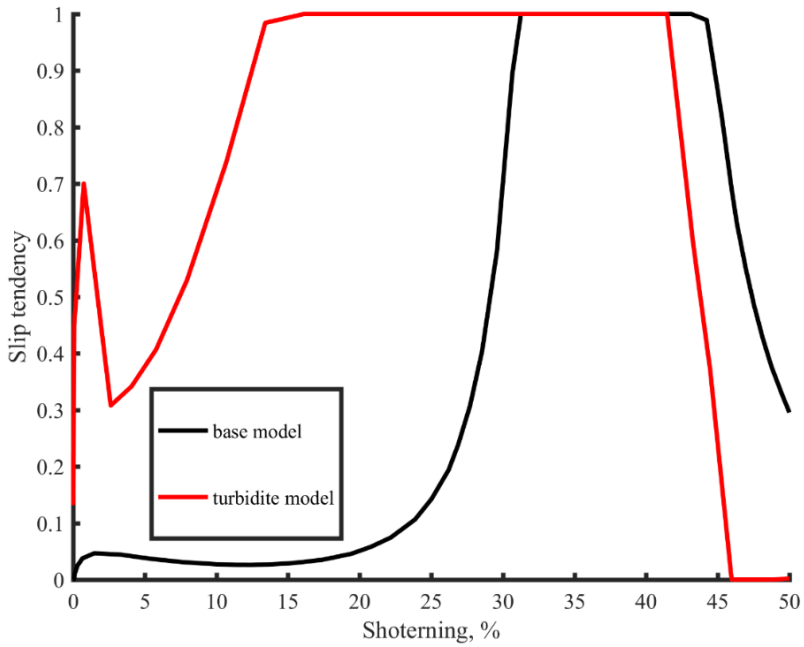

Figure 4.1. Slip tendency of the true multilayer models based on turbidite sequence setups based on sinusoidal initial perturbations.

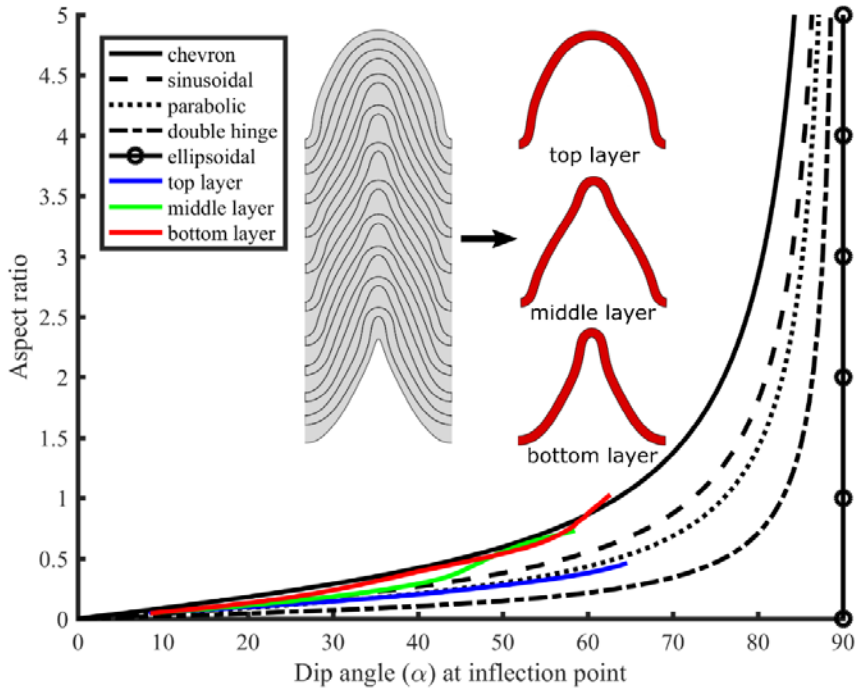

Figure 4.2. The varying fold profiles from culminate to termination based on turbidite sequence.

4.3.2. Initial Wavelength. In the model of effective single layer setups, the initial wavelength follows Schmalholz and Podladchikov (1999) and Schmalholz et al. (2001) dominant wavelength theory and no chevron folds develop based on initial perturbations, competence contrast and friction coefficient. Field observations and seismic studies suggest that sediment waves are variable and exist in the deep ocean (i.e. Posamentier, 2003) or the outcrops (i.e. Ponce and Carmona, 2001; Campion et al, 2010). In Campion et al.'s (2010) study, no competence contrast between each layer and the ratio of sediment wavelength to associated layer thickness is 19. It is smaller than the ratio of effective single layer model in this study ($\frac{\mathbf{10\%}\ \boldsymbol{of\ dominant\ wavelength}}{\boldsymbol{associated\ layer\ thickness}} = \mathbf{170}$). In order to correspond to the field data, 10% of dominant wavelength is used to investigate the effect of initial wavelength (the results are shown in Figure 4.3).

The results are different with other chevron folding models and partly correspond to the kinematic models from De Sitter (1964) and Pollard and Fletcher (2005). The timing of slip is during the early stages and resulting folds is non-hinge collapse chevron folds. However, the fold profiles show that limbs are becoming thinner and hinge zones are becoming thicker during the deformation, which indicates that both flexural slip and flexural flow play important roles during the development of chevron folds. The evolution of folding is different to the true multilayer setups with flexural slip that folding geometry transforms from sinusoidal to chevron gradually and at the end of folding the dip angle at inflection point does not remain constant.

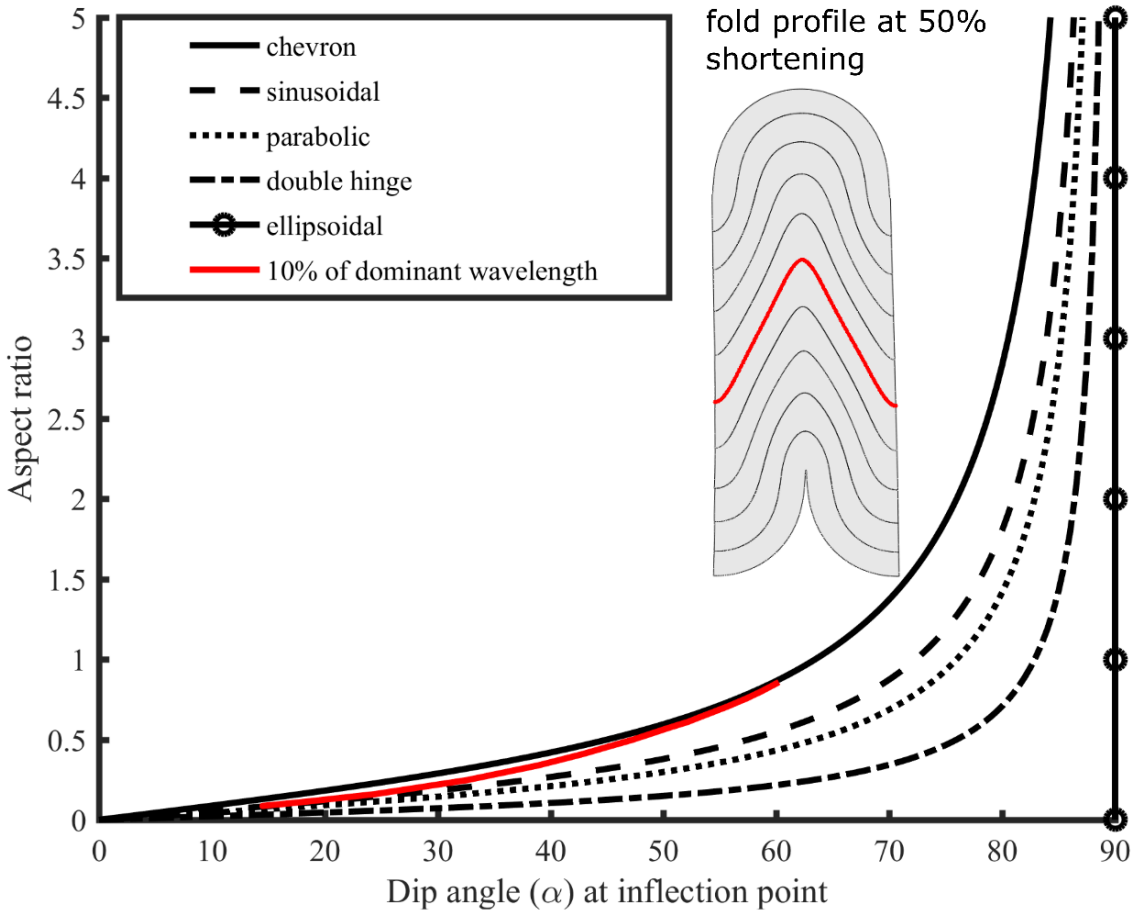

Figure 4.3. The relationship between aspect ratio and dip angle at the inflection point featuring 10% of dominant wavelength based on sinusoidal initial perturbations. Red lines in the fold profiles highlight the location of calculating aspect ratio.

5. CONCLUSIONS

This study represents an extensive quantitative data set of flexural slip during the development of multilayer chevron folds and provides detailed information about the spatial and temporal evolution of the slip. Especially, this paper extend more details of the slip and fold profile evolution by comparing with kinematic models, plasticine models, and field observations. The results show that:

In effective single layer setups, chevron folds do not develop with varying initial perturbation, viscosity contrast between matrix and folding layers and friction coefficient (white noise initial perturbations) based on dominant wavelength. However, if the initial wavelength reduces to shorter according to sedimentary observations (e.g. 10% of dominant wavelength), chevron folds without hinge collapse develop. The information of slip tendency and folds profiles with the location of maximum cumulative slip suggests that slip initiates during the early stages of folding and large amount of slip occur at the inflection points. In addition, the evolution of fold profiles imply that flexural slip in effective single layer setups favor the development of double hinge (box) folds.

In true multilayer setups, all models reproduce the chevron folds with hinge collapse. As the fraction of incompetence decreases, the number of slip surfaces increases. Slip initiates during the later stages of folding, terminates before the folds lock up and large amount of cumulative slip occur near the hinge zones. Form the evolution of fold profiles, all the chevron folds transform from sinusoidal initial seed folds. In addition, combining with the aspect ratio vs. dip angle plots, it imply that flexural slip in true multilayer setups favor the transform from sinusoidal to chevron folds. Moreover, because of frequency of

turbidite sequences of chevron folds in field observations, alternating permeable models are involved. The results show that turbidite sequence make the timing of slip initiation ahead of time because of overpressure.

6. FUTURE WORK

The main limitation of this study relates to the dominant wavelength definition. From both effective single layer and true multilayer models based on white noise initial perturbations, different dominant wavelength can be observed in the low friction coefficient model. Other limitations would be the consideration of surface conditions. In this study, the overburden load is applied as 500, 1000 and 2000 meters thickness. However, at the surface conditions, the viscoelastic rheology is not valid and a different approach would be necessary to investigate the “sticky air”.

Future work firstly include the consideration of the dominant wavelength based on white noise initial perturbations and study the controlled mechanisms. In addition, different approach should be used to setup shear viscosity models to simulate the role of flexural slip in the development of fold at surface conditions. At last, non-cylindrical folds would have to be considered to understand the implications of three dimensional slip. All these considerations increase significantly the computational work and would require a combination of finite element code along with a robust cluster of computer.

APPENDIX A.

SLIP TENDENCY DEFINITION

The slip tendency parameter (Morris et al., 1996), Ω, is defined as the following ratio:

$$\Omega = \frac{\tau_s}{\sigma_n \mu}$$

where τ_s is the shear stress, σ_n is the normal stress and μ is the friction coefficient at a given frictional interface location. While slip tendency is commonly used to indicate the likelihood of a preexisting failure plane to initiate slip, in this study slip tendency is also used to identify the time period during which slip occurs. A magnitude of Ω=1 indicates that slip is taking place, while smaller values represents that the frictional interface remains "welded". The slip tendency ratio is valuable to identify the spatial and temporal slip evolution for each bedding surface included in the models.

APPENDIX B.

DERIVATION OF THE FOLD PROFILES

Table B.1 shows the relationship between aspect ratio ($aspect\ ratio = \frac{2\times amplitude}{wavelength}$) and dip angle at the inflection point used to assess the resulting fold shape and to confirm the development of chevron folds (Ghassemi et al., 2010).

Table B.1. General functions and relationships between aspect ratio and dip angle at inflection point for different fold geometries used in this study for analyzing fold geometry.

Fold type	General function	Aspect ratio vs. dip angle at inflection point
Chevron	$y = 2px$	$\alpha = arctan(2p)$
Sinusoidal	$y = 2psin(\frac{\pi}{2x})$	$\alpha = arctan(\pi pcos\left(\frac{\pi}{2x}\right))$
Parabolic	$y = 2p(2x - x^2)$	$\alpha = arctan(4p - 4px)$
Ellipsoidal	$y = 2p(2x - x^2)^{0.5}$	$\alpha = arctan(2(2x - x^2)^{-0.5}(1 - x))$
Double hinge (box)	$y = 2p(1 - (1 - x)^2)$	$\alpha = arctan(-24px + 8p + 24px^2 - 8px^3)$

APPENDIX C.

RESULTS FOR THE BASED MODEL

In this appendix, two figures show the resulting folds of varying friction coefficient and overburden loads based on sinusoidal initial perturbations (Damasceno et al., 2017). Slip evolution and deformed fold profiles for the base models featuring varying friction coefficients of the folding layer interfaces (Models 1, 1a, 1b) based on sinusoidal initial perturbations are shown in Figure C.1. For the high friction coefficient model (Model 1; green line), slip initiates during the early stages (~7% shortening), terminates after 25% of shortening. For the mid friction coefficient model (Model 1a; red line), slip initiates during the early stages (~5% shortening), terminates after 32% shortening. For the low friction coefficient model (Model 1b; blue line), slip initiates during the early stages (~3% shortening), and terminates until the end of folding. For all models, the locations of the maximum cumulative amount of slip are near the inflection points and it can be observed that no chevron folds is formed.

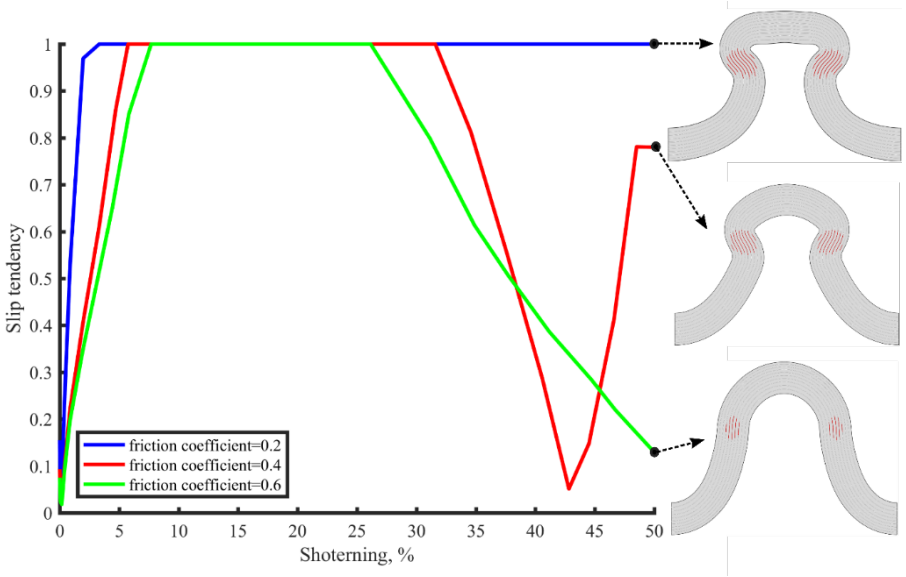

Figure C.1. Slip tendency evolution featuring varying friction coefficients based on sinusoidal initial perturbations. Red lines in the fold profiles highlight the location of maximum cumulative slip.

Slip evolution and deformed fold profiles for the base models featuring varying overburden loads (Models 1, 1c, 1d) based on sinusoidal initial perturbations are shown in Figure C.2. For the low overburden model (Model 1c; blue line), slip initiates during the early stages (~3% shortening), terminates after 32% of shortening. For the mid overburden model (Model 1; red line), slip initiates during the early stages (~5% shortening), terminates after 26% shortening. For the high overburden model (Model 1d; green line), slip is not initiated and flexural flow dominates. For all models, the locations of the maximum cumulative amount of slip are near the inflection points and it can be observed that no chevron folds is formed.

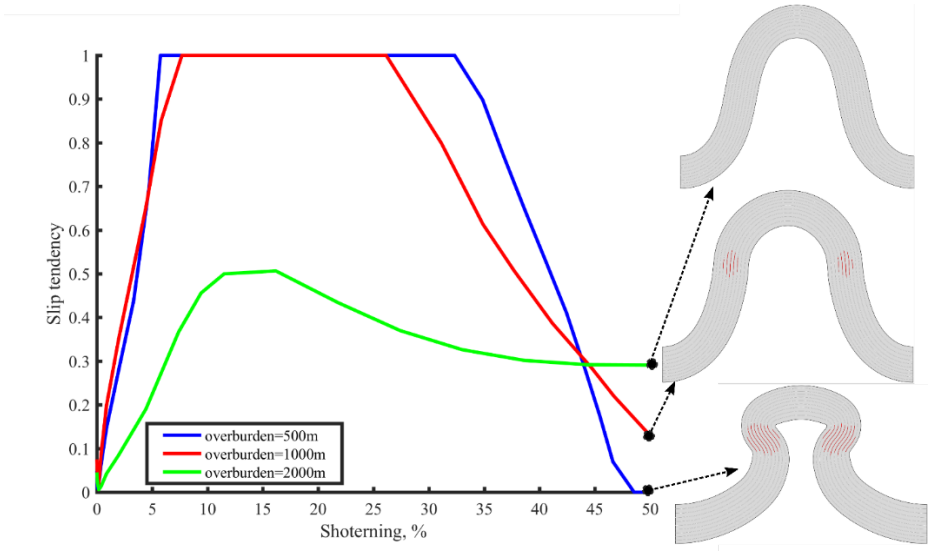

Figure C.2. Slip tendency evolution featuring varying overburden loads based on sinusoidal initial perturbations. Red lines in the fold profiles highlight the location of maximum cumulative slip.

BIBLIOGRAPHY

Bayly, M.B., 1970. Viscosity and anisotropy estimates from measurements on chevron folds. *Tectonophysics 9,* 459-474.

Bayly, M.B., 1974. An Energy Calculation Concerning the Roundness of Folds. *Tectonophysics 24,* 291-316.

Bastida, F., Aller, J., Toimil, N.C., Lisle, R.J., Bobillo-ares, N.C., 2007. Some Considerations on the Kinematics of Chevron Folds. *Journal of Structural Geology 29,* 1185-1200.

Behzadi, H., Dubey, A.K., 1980. Variation of interlayer slip in space and time during flexural folding. *Journal of Structural Geology 2,* 453-457.

Biot, M.A., Willis, D.G., 1957. The Elastic Coefficients of the Theory of Consolidation. *Journal of Applied Mechanics*.

Biot, M.A., 1965. *Mechanics of Incremental Deformations,* John Wiley and Sons, New York.

Blay, P., Cosgrove, J.W., Summers, J.M., 1977. An Experimental Investigation of the Development of Structures in Multilayers under the Influence of Gravity. *Journal of the Geological Society 133,* 329-342.

Cobbold, P.R., 1976. Mechanical effects of anisotropy during large finite deformation. *Bulletin de la Société géologique de France 18,* 1497e1510.

Cobbold, P.R., Cosgrove, J.W., Summer J.M., 1971. Development of Internal Structure in Deformed Anisotropic Rocks, *Tectonophysics 12,* 23-53.

Chapple, W.M., 1969. Fold Shape and Rheology: the Folding of an Isolated Viscous-plastic Layer. *Tectonophysics 7,* 97-116.

Chapple, W.M., 1970. The finite-amplitude instability in the folding of layered rocks. *Canadian Journal of Earth Sciences 7,* 457-466.

Chapple, W.M., Spange, J.H., 1974. Significance of Layer-parallel Slip during Folding of Layered Sedimentary Rocks. *Bullet of Geological Society of America 85,* 1523-1534.

Colman-sadd, S.P., 1978. Fold Development in Zagros Simply Folded Belt, Southwest Iran. *AAPG Bulletin 62,* 984-1003.

Couples G.D., Lewis, H., 1998. Lateral Variations of Strain in Experimental Forced Folds. *Tectonophysics 295,* 79-91.

Damasceno, D.R., Eckert, A., Liu, X., 2017. Flexural-Slip during Visco-elastic Buckle Folding. *Journal of Structure Geology 100,* 62-76.

De Sitter, L.U., 1964. *Structural Geology*. McGraw Hill, New York.

Dubey, A.K., Cobbold, P.R., 1977. Noncylindrical Flexural Slip Folds in Nature and Experiment. *Tectonophysics 38,* 223-239.

Eckert, A., Connolly, P.T., 2007. Stress and Fluid-flow Interaction for the Coso Geothermal Field Derived From 3D Numerical Models.

Eckert, A., Connolly, P. & Liu, X. 2014. Large-scale Mechanical Buckle Fold Development and the Initiation of Tensile Fractures. *Geochemistry, Geophysics, Geosystems 15,* 4570-4587.

Eckert, A., Liu, X. & Connolly, P. 2015. Pore Pressure Evolution and Fluid Flow during Visco-elastic Single-layer Buckle Folding. *Geofluids 16,* 231-248.

Fletcher, C.R., Pollard, D.D., 1999. Can We Understand Structural and Tectonic Processes and Their Products without Appeal to a Complete Mechanics? *Journal of Structural Geology 21,* 1071-1088.

Fowler, T.J., Winsor, C.N., 1996. Evolution of Chevron Folds by Profile Shape Changes: Comparison between Multilayer Deformation Experiments and Folds of the Bendigo-Castlemaine Goldfields, Australia. *Tectonophysics 258,* 125-150.

Fowler, T.J., Winsor, C.N., 1997. Characteristics and Occurrence of Bedding-Parallel Slip Surfaces and Laminated Veins in Chevron Folds from the Bendigo-Castlemaine Goldfields: Implications for Flexural-Slip Folding. *Journal of Structural Geology 19,* 799-815.

Ghosh, S.K., 1968. Experiments of Buckling of Multilayers Which Permit Interlayer Gliding. *Tectonophysics 6,* 207-249.

Ghassemi, M. R., Schmalholz, S. M., Ghassemi, A. R., 2010. Kinematics of Constant Arc Length Folding for Different Fold Shapes. *Journal of Structural Geology 32,* 755-765.

Hehzadi, H., Dubey, A.K., 1980. Variation of Interlayer Slip in Space and Time during Flexural Folding. *Journal of Structural Geology 2,* 453-457.

Hills, E.S., 1972. *Elements of Structural Geology (2nd edn).* Chapman and Hall, London.

Honea, E., Johnson, A.M., 1976. A Theory of Concentric, Kink and Sinusoidal Folding and of Monoclinal Flexuring of Compressible, Elastic Multilayers: IV. Development of Sinusoidal and Kink Folds in Multilayers Confined by Rigid Boundaries. *Tectonophysics 30,* 197-239.

Horne, R., Culshaw, N., 2001. Flexural Slip Folding in the Meguma Group, Nova Scotia, Canada. *Journal of Structural Geology 23,* 1631-1652.

Hudleston, P.J., 1973. Fold Morphology and Some Geometrical Implications of Theories of Fold Development. *Tectonophysics 16,* 1-46.

Hudleston, P.J., Treagues, S.H., Lan, L., 1996. Flexural Flow Folding: Does It Occur in Nature? *Geology 24*, 203-206.

Jaeger, J. C., Cook, N. G. W., Zimmerman, R., 2007. *Fundamentals of Rock Mechanics,* Blackwell.

Johnson, A.M., Honea, E., 1975. A Theory of Concentric, Kink, and Sinusoidal Folding and of Monoclinal Flexuring of Compressible, Elastic Multilayers: III. Transition from Sinusoidal to Concentric-like to Chevron Folds. *Tectonophysics 27,* 1-38.

Lan, L., Hudleston, P., 1996. Rock rheology and sharpness of folds in single layers. *Journal of Structural Geology 18,* 925-931.

Latham, J.P., 1985. A Numerical Investigation and Geological Discussion of the Relationship between Folding, Kinking and Faulting. *Journal of Structural Geology 7*, 237-249.

Mancktelow, N.S., 1999. Finite Element Modeling of Single Layer Folding in Elasto-viscous Materials: The Effect of Initial Perturbation Geometry, *Journal of Structure Geology 21,* 161-177.

Morris, A.P., Ferrill, D.A., Henderson, D.B., 1996. Slip Tendency Analysis and Fault Reactivation. *Geology 24,* 275-278.

Nur, A., Byerlee, J.D., 1971. An exact effective stress law for elastic deformation of rock with fluids. *Journal of Geophysical Research 76,* 6414-6419.

Pollard, D.D., Fletcher, R.C., 2005. *Fundamentals of Structural Geology,* Cambridge University Press, New York.

Price, N.J., Cosgrove, J.W., 1990. *Analysis of Geological Structures,* Cambridge University Press, Great Britain.

Ramsay, J.G., 1967. *Folding and Fracturing of Rocks.* McGraw Hill, New York.

Ramsay, J.G., 1974. Development of chevron folds. *Geological Society of America Bulletin 85,* 1741-1754.

Ramsay, J.G., Huber, M.I., 1987. *The Techniques of Modern Structural Geology. In: Folds and Fractures, vol. II,* Academic Press, London.

Ridley, J., Casey, M., 1989. Numerical Modeling of Folding in Rotational Strain Histories: Strain Regimes Expected in Thrust Belts and Shear Zones. *Geology 17,* 875-878.

Sanz, P.F., Pollard, D.D., Allwardt, P.F., Borja, R.I., 2008. Mechanical Models of Fracture Reactivation and Slip on Bedding Surfaces during Folding of the Asymmetric Anticline at Sheep Mountain, Wyoming. *Journal of Structural Geology 30,* 1177-1191.

Schmalholz, S. M., Podladdchikov, Y., 1999. Buckling versus Folding: Importance of Viscoelasticity. *Geophysical Research Letters 26,* 2641-2644.

Schmalholz, S.M., Podladdchikov, Y.Y., and Schmid, D.W., 2001. A Spectral Finite Difference Method for Simulating Large Deformations of Heterogeneous, Viscoelastic Materials, *Geophysical Journal International 145,* 199–208.

Schmid, D.W., Podladdchikov, Y.Y., 2006. Fold Amplification Rates and Dominant Wavelength Selection in Multilayer Stacks. Philosophical Magazine 86, 3409-3423.

Smart, K. J., Ferrill, D. A., Morris, A. P., 2009. Impact of Interlayer Slip on Fracture Prediction from Geomachanical Models of Fault-related Folds. *AAPG Bulletin 93,* 1447-1458.

Tanner, P.W.G., 1989. The flexural-slip Mechanism. *Journal of Structural Geology 11,* 635-655.

Tanner, P.W.G., 1992, Morphology and Geometry of Duplexes Formed during Flexural-slip Folding. *Journal of Structural Geology 14,* 1173-1192.

Twiss, R. J., Moores, E. M., 1973. *Structural Geology*, Freeman.

Twiss, R.J., 1988. Description and classification of folds in single surfaces. *Journal of Structural Geology 10,* 607-623.

Weijermars, R., 1992. Progressive Deformation in Anisotropic Rocks. *Journal of Structural Geology 14,* 723-742.

Williams, J.R., 1980. Similar and Chevron Folds in Multilayers Using Finite Element and Geometric Models. *Tectonophysics 65,* 323-338.

Zhang, Y., Mancktelow, N.S., Hobbs, B.E., Ord, A., Muhlhaus, H. B., 2000. Numerical Modeling of Single-layer Folding: Clarification of an Issue Regarding the Possible Effect of Computer Codes and the Influence of Initial Irregularities, *Journal of Structure Geology 22*, 1511–1522.

VITA

Yuxing Wu was born in Xi'an, Shaanxi, China. He has been through exchange study program to Missouri University of Science and Technology in August, 2013. He earned his Bachelor's degree in Petroleum Engineering from both China University of Geosciences and Missouri University of Science and Technology in May, 2016. Yuxing was accepted in the Petroleum Engineering Master program at Missouri University of Science and Technology in August, 2016. During his Master's study, he worked with Dr. Andreas Eckert as grader for the classes of Mechanical Earth Modelling. His research was worth a manuscript for publication. Yuxing received his Master's degree in Petroleum Engineering in May 2018 from Missouri University of Science and Technology.